LITHIUM MAS NMR STUDIES OF LITHIUM ION ENVIRONMENT AND ION DYNAMIC PROCESS IN LITHIUM IRON AND MAGNESIUM PYROPHOSPHATE AS NEW SERIES OF CATHODE MATERIAL FOR LITHIUM ION BATTERIES

LITHIUM MAS NMR STUDIES OF LITHIUM ION ENVIRONMENT AND ION DYNAMIC PROCESS IN LITHIUM IRON AND MAGNESIUM PYROPHOSPHATE AS NEW SERIES OF CATHODE MATERIALS FOR LITHIUM ION BATTERIES

BY

XUAN HE, B. SC.

A Thesis Submitted to the School of Graduate Studies in Fulfillment of the Requirements for the Degree of Master

McMaster University

McMaster University MASTER(2012) Hamilton, Ontario(Chemistry)

TITLE: Lithium MAS NMR Studies of Lithium Ion Environment and Ion Dynamic Process in Lithium Iron and Magnesium Pyrophosphate as New Series of Cathode Materials for Lithium Ion Batteries

AUTHOUR: Xuan He, B. Sc. (Tsinghua University)

SUPERVISOR: Professor G.R.Goward

NUMBAER OF PAGES: xx, 113

ABSTRACT

Lithium-ion batteries provide a more cost-effective and non-toxic source of reusable energy compare to other energy sources. Several research studies have lead to production of some more promising cathode components for lithium ion batteries. Recently, a new series of pyrophosphate-based composition $Li_2FeP_2O_7$ and $Li_2MnP_2O_7$ has been reported as cathode materials. They have shown a 3D framework structure and the two Lithium-ions in the three-dimensional tunnel structure make it possible that more than one lithium ion be extracted during cycling. Lithium solid state nuclear magnetic resonance (NMR) is an effective technique to study this cathode material, not only for analyzing local structure, but also for investigation of the microscopic processes that take place in the battery. In this work, $Li_2FeP_2O_7$ and $Li_2MnP_2O_7$ have been synthesized. The lithium environment of these materials is studied using 1D ^{6,7}Li NMR. Assignment of $Li_2MnP_2O_7$ spectrum has been made based on Fermi-contact interaction and crystal structure. Both variable temperature experiment and 1D selective inversion NMR are used to establish Li-ion pathways as well as Li hopping rates for $Li_2MnP_2O_7$. Also, ^{7}Li MAS NMR measurements are used to characterize Li environments in $LixFeP_2O_7$ after being electrochemically cycled to different points, and preliminary results regard to changes to ion mobility in $LixFeP_2O_7$ at different electrochemical cycled points are presents here, solid-solution (de)lithetiation process is confirmed for this material.

Table of Content

ABSTRACT……iii

Table of Content……..……..……...iv

List of Tables……ix

List of Figures……....x

List of Abbreviations and Symbols……xv

Chapter 1: Introduction of Lithium-Ion Battery…….……1

1.1 Motivation of the thesis…… …1

1.2 Basic Principle for Lithium Ion Batteries.…… …2

1.3 Studied Cathode Materials in Thesis…… ……7

1.3.1 $Li_2MnP_2O_7$……...…… ……8

1.3.2 $Li_2FeP_2O_7$……..…… ……..…10

1.4 Summary……..…… ……...…11

1.5 Reference……..…… ……...…12

Chapter 2: Introduction of Solid-State NMR and NMR Techniques Used in Thesis……...15

2.1 Spin properties of Nuclei and Unpaired Electrons in Applied Magnetic Field...15

2.2 Spin Relaxation…….…..……17

2.4.1 Spin-Lattice Relaxation…….…….…..……17

2.4.2 Spin-Spin Relaxation…….…….…..……20

2.3 Lithium NMR Spectra of Cathode Materials.…….…..……..…22

2.4 NMR of Paramagnetic Cathode Materials.…….…..……..…24

2.4.1 Fermi-Contact Interaction.……..…….…..……..…24

2.4.2 Dipolar Coupling.……..……..…….…..……..…26

2.5 One-Dimensional Selective Inversion Experiment…..…….……..…27

2.5.1 Introduction to other SSNMR techniques used in dynamic study…..….27

2.5.2 Introduction of One-Dimensional Selective Inversion Experiment……...28

2.5.3 CIFIT Used for Data Fit……..……..…….……..…32

2.5.4 Shaped Pulse Selective Inversion Experiments…..…….……..…34

2.6 Summary……..…….…….……...…35

2.7 References……..…….…….…….……...…35

Chapter 3: Structure Information and Quantification of Li Ion Mobility of $Li_2MnP_2O_7$ Using ^{6,7}Li MAS Measurement…….37

3.1 Introduction……..…….…….……..……37

3.2 Experimental…….. ……..…….…….…..…..……40

3.2.1 Sample Preparation…….…….…….…..…..……40

3.2.2 Powder XRD ……..…….…….…..…..……41

3.2.3 Solid-State NMR.……..……..…….…..…..……43

3.2.4 1D Selective Inversion Data Analysis…..…….…..…..…..…44

3.3 Result and Discussion.……..……..…….…..…..…..…45

3.3.1 ^{6,7}Li MAS NMR of $Li_2MnP_2O_7$……..…….…..…..…..…45

3.3.2 Site Assignment of $Li_2MnP_2O_7$……..…….…..…..…..…46

3.3.3 1D Variable Temperature Measurements……..…….…..…..…50

3.3.4 Quantification of Ion Dynamics in $Li_2MnP_2O_7$ using ^6Li 1D Shaped Pulse Selective Inversion Experiments.…….……...…..…53

3.3.5 Identification of Ion Exchange Pairs…..……...……...…63

3.4 Summary…..……...……...…….67

3.5 References.……...……...……..69

Chapter 4: Structure Information and Quantification of Li Ion Mobility of $Li_2FeP_2O_7$….....……...……...…….71

4.1 Introduction.……...……...……...…….71

4.2 Experimental……...……...……...…….81

4.2.1 Sample Preparation…...……...…….…….81

4.2.2 Powder XRD …...…….……...…….…….82

4.2.3 Electrochemical Measurements……...…….…..…….84

4.3 Result and Discussion……..……...……...……..…….85

4.3.1 ^{6,7}Li MAS NMR of $Li_2FeP_2O_7$……...……...……..…….86

4.3.2 ^{7}Li MAS Study of Electrochemically Cycled $Li_xFeP_2O_7$…..….91

4.4 Summary……..……...……...……..…….…104

4.5 References…….……....……...……..…….…105

Chapter 5: Summary and Future Direction…...…….……..…….…...106

5.1 Summary and Outlook……...……...……..…….…….106

5.2 References…….……...……...……..…….…113

List of Tables

Table 2.1- spin numbers and gyromagnetic ratios for nuclei……..17

Table 3.1- Jump frequency and correlation time for AB exchange pair……..51

Table 3.2- Summary of Li environments in $Li_2MnP_2O_7$…….….52

Table 3.3-Different input rate that affects the output rate fit by CIFIT…….…..55

Table 3.4- Different pulse length and the exchange rates fit by CIFIT…….……..58

Table 3.5- Summary of all possible exchange pairs in $Li_2MnP_2O_7$…….……64

List of Figures

Figure 1.1-Plot of volumetric and gravimetric energy densities of different battery…3

Figure 1.2- schematic of lithium ion battery…….6

Figure 1.3- Polyhedral representation of the 3D structure of $Li_2MnP_2O_7$ ……...…….9

Figure 2.1- Pulse sequence for T_1 inversion-recovery method……..…….19

Figure 2.2- sample by Magic Angle Spinning……...……..23

Figure 2.3- Polarization and Delocalization mechanism…….25

Figure 2.4- Pulse sequence for shaped pulse selective inversion experiment as well as the Spectrum of $Li_2MnP_2O_7$ at different mixing time when invert C…….31

Figure3.1- Environment of the lithium cations in $Li_2MnP_2O_7$……38

Figure 3.2-XRD pattern of product after first step (top) and XRD pattern of $Li_2MnP_2O_7$ (bottom)…….42

Figure 3.3-^{6}Li and ^{7}Li MAS spectra of $Li_2MnP_2O_7$, * refer to spinning sidebands…46

Figure 3.4- Deconvolution for ^{7}Li MAS spectra of $Li_2MnP_2O_7$ …….48

Figure 3.5- Polarization and Delocalization mechanism…….48

Figure 3.6-Lithium coordination environments in $Li_2MnP_2O_7$. The Mn centers depicted are found in the second coordination sphere and are responsible for transfer positive spin density to the Li nucleus. The lithium atoms are shown in different red, oxygen atoms in grey, and Mn in blue. as well as the Crystal structure data of $Li_2MnP_2O_7$……...……49

Figure 3.7- Plot of chemical shift to temperature for each resonance as well as the ^6Li MAS spectrum obtained at VT…….51

Figure 3.8- Two identified exchange pair from crystal structure data as well as the crystal structure of $Li_2MnP_2O_7$……...……52

Figure 3.9-Pulse sequence for shaped pulse selective inversion experiment……..….56

Figure 3.10- Plot integration to mixing time of resonance C when invert D at different temperature…….59

Figure 3.11- Plot integration to mixing time of resonance D for selective invertion data(above) and Non selective invertion data(bottom)……..60

Figure 3.12- Activation energy fit for CD exchange pair. Exchange rate at variable temperatures are shown below……...61

Figure 3.13- Plot integration to mixing time of resonance A when invert resonance B for selective invertion data as well as comparasion of initial spectra and spectra after B is inverted…….…….62

Figure 3.14- Two identified exchange pair from crystal structure data as well as crystal structure of $Li_2MnP_2O_7$……...63

Figure 3.15- Crystal structure for $Li_2MnP_2O_7$, with red for Li1, pink for Li2, purple for Li3 and green for Li4. Mn is in blue and P is in yellow……...66

Figure 4.1-Electrochmical curve of voltage to x shown two-phase reaction……..73

Figure 4.2-Electrochmical curve of voltage to x shown solid-solution process…..…74

Figure 4.3- XRD patterns of cycled $Li_{2-x}FeP_2O_7$ in charge(a) and discharge(b) by Kim et.al……..…….76

Figure 4.4- XRD patterns of cycled $Li_{2-x}FeP_2O_7$ by Shimizu et al…….…….78

Figure 4.5- Zoom in XRD patterns of cycled $Li_{2-x}FeP_2O_7$ by Shimizu et al…..…….79

Figure 4.6- Open circuit voltage curves for $Li_2FeP_2O_7$…..…….79

Figure 4.7-Comparision of XRD pattern and unit cell parameters for $LiFeP_2O_7$ and $Li_2FeP_2O_7$..……..…….81

Figure 4.8-refined X ray diffraction(XRD) pattern of synthesized $Li_2FeP_2O_7$, red line is the calculated result, while the black line shows the experiment data. Blue line indicates the difference map……...83

Figure 4.9- Charge and discharge curve for synthesized $Li_2FeP_2O_7$……. ,,,,,,,,,,,,,,..85

Figure 4.10-^{7}Li NMR spectrum of synthesized $Li_2FeP_2O_7$ …….…...86

Figure 4.11- deconvolution spectrum and integration result for $Li_2FeP_2O_7$ synthesized by two methods...……...87

Figure 4.12-^{7}Li NMR spectrum of the as-prepared $Li_2FeP_2O_7$ and the cycled material. The blue area corresponding to peaks arising from Fe^{2+}, black area corresponding to peaks arising from Fe^{3+}……..89

Figure 4.13- ^{7}Li MAS spectrum for $LiMnPO_4$ and $LiFePO_4$……..……91

Figure 4.14-Deconvolution of ^{7}Li NMR spectrum of the $Li_{1.3}FeP_2O_7$ o, A refer to the narrow resonance arising from Fe^{3+}, while B refer to the broad resonance arising from Fe^{2+}……95

Figure 4.15- electrochemical experiments of the coin cells for $Li_2FeP_2O_7$ with the stopping shown on the figure(above), Relative Integration values for “narrow” peaks(Fe^{3+}) and “broad” peaks(Fe^{2+}) (bottom)……...97

Figure 4.16-Schematic detailing the local Li environment with respect to Fe transition metal center proximity for $LiFeP_2O_7$. Left: geometry data for Li site ; Right: Local Li environments for lithium site……..…….....98

Figure 4.17-Schematic detailing the local Li environment with respect to Fe transition metal center proximity for $Li_2FeP_2O_7$. Left: geometry data for 4 Li sites ; Right:

Local Li environments for each lithium site ……..……...….101

Figure 4.18-Structure of $Li_{1.6}FeP_2O_7$, one unit cell…….……...……...….103

List of Abbreviations and Symbols

SSNMR	Solid State Nuclear Magnetic Resonance
MAS	Magic Angle Spinning
VT	Variable Temperature
EXSY	Exchange Spectroscopy
SI	Selective Inversion
NSI	Nonselective Inversion
EV	Electric Vehicle
V	Volt
Z	Atomic number
I	Spin quantum number
B_0	Applied magnetic field strength
w_0	Larmor frequency
γ_N	Nuclear gyromagnetic ratio

γ_e	Electron gyromagnetic ratio
τ_r	Rotor period
H	Hamiltonian
<Sz>	Unpaired electron spin density
Dij	Dipolar coupling constant
CSA	Chemical Shift Anisotropy
ppm	Part per million
FWHM	Full-Width at Half-Maximum
T_1	Spin-lattice relaxation time
T_2	Spin-spin relaxation time
k	Ion hopping rate
Ea	Activation energy

Chapter 1: Introduction of Lithium-Ion Battery

1.1 Motivation of the thesis

The objective of this thesis is applying solid-state Nuclear Magnetic Resonance(SSNMR) techniques to investigate the structural features and lithium ion mobility pathways in a series of lithium pyrophosphate materials used as positive electrodes in lithium ion batteries (LiBs). In this report, Chapter 1 gives an introduction of current lithium ion battery technology, and details the structural and electrochemical properties of cathode materials studied in this thesis. Chapter 2 includes an introduction of solid-state NMR and a description of SSNMR experiments that have been used here to investigate the structural and ion mobility properties of the cathode materials in this thesis. Chapter 3 demonstrates the use of ^{6,7}Li variable temperature(VT) method and 1D selective inversion experiments to investigate ion mobility and study Li ion hopping pathways in $Li_2MnP_2O_7$. Chapter 4 characterizes the electrochemical extraction of $Li_2FeP_2O_7$, cycled cathode material($Li_xFeP_2O_7$) at different stopping points have been studied in this chapter. The final Chapter provides a summary and proposes future work for research in thie field.

1.2 Basic Principle for Lithium Ion Batteries

Because they offer the highest energy density among the portable energy sources[1], lithium ion batteries have been widely applied to electronic devices, such as labtops, mobile phones. Figure 1.1[2] clearly shows that lithium ion battery have advantages in both volumetric and gravimetric energy density compared to more traditional batteries including lead-acid and nickel metal hydride systems. Most recently, more and more attention has been attracted to the application of lithium ion battery systems into electric vehicles(EV), which have an electric motor that almost replaces the traditional combustion engine[3]. In order to improve the efficiency of energy transfer for these EV motors, a cheaper, safer and more efficient lithium battery systems is needed. Despite the fact that great success is achieved for lithium ion battery system used in portable electronic devices, many of the cost, lifetime, and safety issues of the current systems still need to be addressed before it will be viable to utlize those systems in larger scale application, such as EVs or grid-level storage.

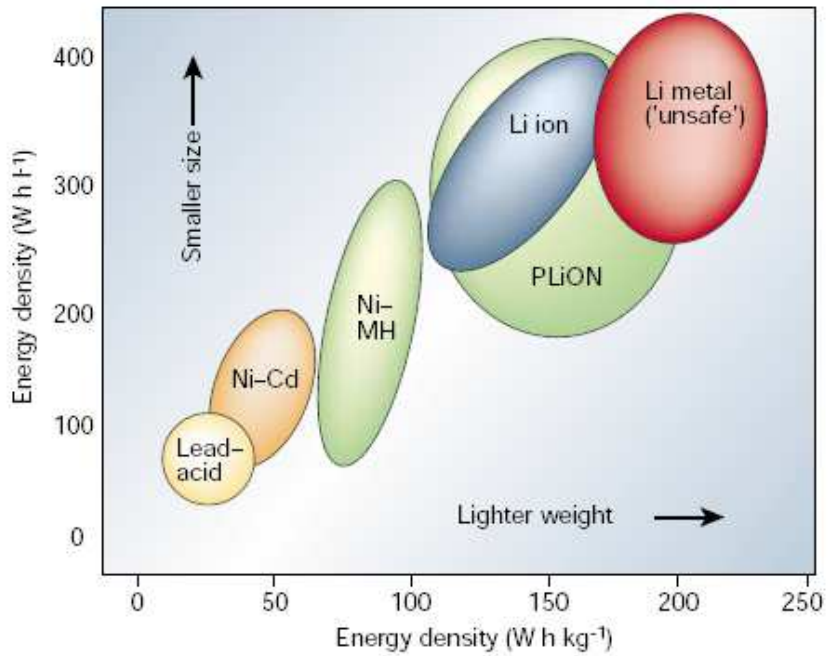

Figure 1.1-Plot of volumetric and gravimetric energy densities of different battery systems

For lithium ion batteries discussed in this report, the schematic is shown in Figure 1.2[4]. In general, Rechargeable lithium ion batteries are source of protable energy where lithium ions flow between two electrodes, separated by electrolyte[5]. And in the systems discussed in this thesis, the positive electrode(cathode) material is the redox active Li intercalation compound(e.g. Li_2FePO_4), while the negative electrode is comprised of a conductive layered material such as graphite[6]. The electrolyte used throughout the thesis is $LiPF_6$. Some basic parameters for describing electrochemical cell will be introduced in the following paragraph.

To describe how fast an electrochemical cell can cycle, the cycling rate capabilities should be introduced. It is a measurement of the time that is needed for the cell to fully charge or discharge[7], and is decribed as C/n. For exanple, a charge rate of C/50, indicates that 50 hours is needed for a fully charge cycle. An idear cathode material should have fast cycling rates in order to obtain high energy output in a certain amount of time.

Both gravimetric volumetric energy density(mAh/g) and gravimetric energy capacity(mAh/cm^3) are used to describe the performance of an electrode material. In general, gravimetric energy capacity is more often reported in literature[8]. Especially in this thesis, only gravimetric energy capacity is used and reported as it is easier to measure in electrochemical experiments. The basic meaning for both values are the measurement of the number of electrons transferred through a circuit either per gram or per volume of the electrode material. The definition of theoretical gravimetric capacity is based on the calculated number of Li ions(or electrons) that are transferred through a circuit per gram of a given cathode material, based on its molar mass, and accessible redox-active phases[9]. However, it's always easy to observe irreversible capacity loss in our experiments, which is mainly because of the reaction between cathode material and electrolyte.

The oxide-based materials: $LiCoO_2$ has been extensively used as positive

electrode material. The battery shown in Figure1.2 represents the most commonly used Li ion battery, with $LiCoO_2$ as the positive elctrode and graphite as the negative electrode. $LiMO_2$ (M = Co, Ni, Mn) family of compounds crystallize in a layered structure. A two-dimensional movement of lithium ions is observed for this series of materials. Even though this material has been commercial used in portable electronic devices, its disadvantages avoid its further application. A significant shortcoming of $LiCoO_2$ is only half of the 280mAh/g theoretical capacity can be reached, as the matials become unstable and structure collapse happen during cycling, which limits its lifetime. What's more, slow charge-discharge rates, high cost, and environmental toxicity do preclude it from use in larger scale application.

The report on the olivine $LiFePO_4$ causes a paradigm shift for cathode materials from oxides to polyanionic compounds[10]. It is shown that the $LiFePO_4$ has a reversible capacity around 162mAh/g(theoretical 170mAh/g) with a Fe^{2+}/Fe^{3+} redox potential of 3.5V, and it is an enviroment friendly, also inexpensive cathode material. The high electrochemical and thermal stability of $LiFePO_4$ as compared to $LiCoO_2$ mainly attribute to its three dimensional (3D) framework structure with PO_4, which then attracted considerable attention. The reason to choose phosphate group is mainly because the strongly covalent P-O bond which create greater ionic character of the Li-O bonds. This offers significant structural support, so that the structure collapse

happened in Li_2CoO_2 can be avoided[11]. Even though the inductive effect from polyanionic groups will reduce the operation voltage. a 3D framework will also offer the practical advantage of increased stability and hence safety. However, since only one Li ion can be extracted from $LiFePO_4$ during electrochemical cycling, this low energy density limits its application to larger scale systems like EVs, HEVs and space ships.

The most recent candidate as cathode materials for LIBs are Nickel, Manganese and Cobalt(NMC) cathode materials[12], which designed as $xLiCoO_2$ $(1-x)LiMn_{1/2}Ni_{1/2}O_2$ $(0<x<1)$. When Co(x) decreases, the thermal stability will increase, while the crystal density, rate capability and material cost will decrease. This series of materials have shown quite high operation voltage(4.2V), which makes them a new, promising candidate as cathode materials for LiBs.

Still, an ideal cathode material with low-cost, high energy density and excellent electrochemical performance is still needed to be discovered.

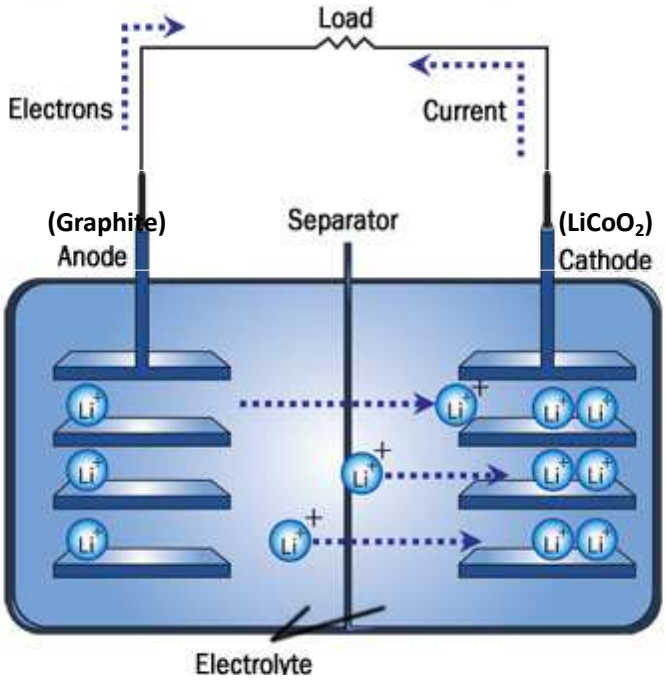

Figure 1.2- schematic of lithium ion battery

1.3 Studied Cathode Materials in Thesis

The coming new energy economy must be based on a cheap and sustainable energy supply. The lithium-ion battery is the most advanced chemical energy storage system, but its safety hazards and difficulty in cost reduction have prohibited large-scale applications. Research in materials science is approaching a solution to these problems by a combination of abundant cheap metal and phosphate group in target cathode materials. These newer cathodes show impressive cycling capabilities and are typically environmentally friendly and economically accessible, with the choice of Fe or Mn transition metals, rather than Co and Ni [13] .

In the search for new lithium-containing cathode materials with cheap transition metal center : Fe, Mn and V, recent studies have focused on changing anions and identified these new pyrophosphate series of compound[13,14,15]. With these new materials however, in order to better understand cycling failure or successes, the behavior of the mobile ion must be understood. While powder X-ray diffraction, as well as a variety of other spectroscopic techniques can provide useful information about structural changes to the lattice during chemical/electrochemical cycling[16], very few techniques can directly monitor the mobile ion. Solid-state nuclear magnetic resonance(SSNMR) is one of these few techniques, where ^{6,7}Li NMR is able to monitor the mobile guest species[17] . Further to this, ^{6,7}Li NMR is sensitive to local site dynamics that take place on the NMR timescale. This includes site-specific rattling and site-to-site Li ion hopping. This will be described in greater detail in Chapter 2.

In this chapter, structural and electrochemical details for both $Li_2FeP_2O_7$ and $Li_2MnP_2O_7$ are introduced.

1.3.1 $Li_2MnP_2O_7$

Recently, a newly synthesized pyrophosphate-based $Li_2MnP_2O_7$ material was

reported[14] . The $Li_2MnP_2O_7$ sample was synthesized in mainly two steps: First Li_2CO_3, MnO and $(NH_4)_2HPO_4$ were mixed in an agate mortar. The mixture was ground for 30 min then heated in air at 600°C for 2 hours and reground. Then the precursor was transferred into an evacuated silica tube, which was heated at 650°C for 15h, after which the product was cooled to 550°C at a rate of 2 °C/h, before being brought back to room temperature. The X-ray powder diffraction analysis indicates that this material has a monoclinic unit cell ($P2_1/a$ space group) with the following parameters: a = 9.8945(1)Å, b = 9.8113(1) Å, c = 11.1596(1) Å, β = 102.485˚(1)[13]. It has a 3D framework built up of manganese polyhedra and phosphate tetrahedra(Figure 1.3) [15]. In the structure, MnO_5 is sharing an edge with MnO_6, which forms Mn_2O_9, and each Mn_2O_9 is then connected with P_2O_7 groups. The structure information obtained by XRD also suggests a quasi two-dimensional network of lithium paths.

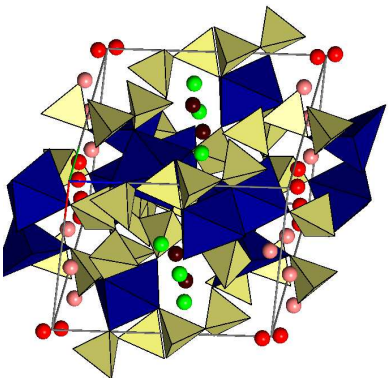

Figure 1.3-Polyhedral representation of the 3D structure of $Li_2MnP_2O_7$

However, this material is electrochemically inactive by now. This may be caused by the poor conductivity of the material or the decomposition of the electrolyte. Nishimura et al.[14] and Zhou et al.[15] find that the Fe version of pyrophosphate, $Li_2FeP_2O_7$, is a promising 3.5 V class cathode material for lithium-ion batteries and can safely deliver high-energy density.

1.3.2 $Li_2FeP_2O_7$

Structural and electrochemical details of this material were first published by Zhou.et.al. Fe atoms occupy three crystallographic sites, Fe1, Fe2 and Fe3. Fe1 is coordinated as FeO_6 octahedra, and Fe2 and Fe3 are coordinated as distorted FeO_5 pyramids. Li atoms are coordinated as LiO_4 tetrahedra or LiO_5 trigonal bipyramids, forming a quasi-two-dimensional network along the b-c plane in the $P2_1/c$ setting, which provides a possible path for Li diffusion. This monoclinic unit cell has lattice parameter: a = 11.01847(4)Å, b = 9.75536(3) Å, c = 9.80517(3) Å, β = 101.5416˚(2)[15] . Our NMR studies, described in Ch. 3 & 4 aim to elucidate these pathways. The gravimetric theoretical capacity is 117mAg/h for $Li_2FeP_2O_7$, which corresponding to one lithium ion extracted during electrochemical process.

For both $Li_2FeP_2O_7$ and $Li_2MnP_2O_7$, the Fe^{3+}/Fe^{4+} and Mn^{3+}/Mn^{4+} redox potential fall outside of the voltage range created by most lithium battery electrolytes used(4.5V) [15], which leads to the result that only the first lithium ion can be cycled by now. However, the cyclic voltammetry study reveals second oxidation peaks, at 5.1 V and 5.3 V for $Li_2FeP_2O_7$ and $Li_2MnP_2O_7$[18], respectively, suggesting that Fe^{3+}/Fe^{4+} and Mn^{3+}/Mn^{4+}redox couples are active, which indicated that the second lithium ion can be cycled if a stable high-voltage electrolyte is found and electronic conductivity is enhanced.

Due to the small scattering factor of Li ion in XRD studies, a disagreement of lithium occupancy appears for obtained structure data reported by different groups[17][18], which need to be confirmed, and also, we are quite interested in how lithium occupancy change by different synthesis methods, and if the different lithium occpancy will give us different ion dynamic. Because the rates of Li ion diffusion ultimately determine the cycling rate for lithium ion batteries, solid-state NMR has been brought into this study here.

1.4 Summary

Even though at this moment, a lot of cost and safety issues are still needed to be

overcome for lithium-ion batteries, they have undergone intensive scientific research and successful applications in a variety of portable electronic devices. And in order to better understand what structural features can enhance or hinder ion diffusion, the determination of the timescales and energy barriers become important. ^{6,7}Li solid-state NMR is a tool that is sensitive to local environments of mobile ion, and it can give us information regarding ion dynamics, which are shown in the following chapters when we applied SSNMR techniques to study particular cathode materials.

1.5 Reference

(1) Whittingham MS, M. Stanley. Chemical Reviews 104 (10): p. 4271–4301.

(2) Tarascon, J.-M.; Armans, M. Nature 2001, 414:p. 359

(3) Nyten, A., et al. Electrochemistry Communications, 2005. 7(2): p. 156-160.

(4) Davis, L.J.M.,.2011. Thesis report: p. 22.

(5) Cahill, L.S., Chapman, R. P., Britten, J. F., Goward, G. R., Journal of Physical Chemistry B, 2 006. 110: p. 7171-7177.

(6) Padhi,A.K., K.S. Nanjundaswamy, and J.B. Goodenough, Journal of the Electrochemical Society, 1997. 144(4): p. 1188-1194.

(7) Kang, B. and G. Ceder, Nature, 2009. 458(7235): p. 190-193.

(8) Morgan, D., A. Van der Ven, and G. Ceder, Electrochemical and Solid State Letters, 2004. 7(2): p. A30-A32.

(9) Zaghib, K., et al., Journal of Power Sources, 2006. 160(2): p. 1381-1386.

(10) Adam, L., A. Guesdon, and B. Raveau, Journal of Solid State Chemistry, 2008. 181(11): p. 3110-3115.

(11) Zhou, H., et al., Chemistry of Materials, 2010. 23(2): p. 293-300.

(12)Y.Sun, C.Ouyang, J.Electrochem. Soc, 2004, 151, A504.

(13) Dominko, R., et al., Electrochemistry Communications, 2006. 8(2): p. 217-222.

(14) Yabuuchi, N., et al., Dalton Transactions, 2010. 40(9): p. 1846-1848.

(15) Yabuuchi, N., et al., Electrochemistry. 78(5): p. 363-366.

(16) Davis, L.J.M., I. Heinmaa, and G.R. Goward, Chemistry of Materials, 2010. 22(3): p.769-775.

(17) Grey, C.P. and N. Dupre, Chemical Reviews, 2004. 104(10): p. 4493-4512.

(18) Kim, J., et al., Journal of the American Chemical Society. 132(47): p. 16825-16840.

(19) Nagaura, T.; Tozawa, K. Prog. Batteries Solar Cells 1990: p.209

Chapter 2: Introduction of Solid-State NMR and NMR Techniques Used in Thesis

2.1 Spin properties of Nuclei and Unpaired Electrons in Applied Magnetic Field

With the rapid development of cathode materials for lithium ion batteries, further information concern about the structural details and ion mobility properties need to be obtained. And ^{6,7}Li Solid-state Nuclear Magnetic Resonance (NMR) is a powerful technique to achieve this target. Therefore, it has been used as the primary method in this thesis. Usually, X-ray diffraction has been used to get structural information, however, XRD is limited by its insensitivity to lithium's low atomic weight, and small scattering factor[1]. While in terms of studying local lithium environments, ^{6,7}Li Solid-state Nuclear Magnetic Resonance (NMR) is more efficient. Furthermore, by studying the different lithium sites involved in the electrochemical process, ^{6}Li/^{7}Li solid-state NMR makes it possible to investigate the dynamics information regarding the mobile Li-ions.

Nuclei are composed of positively charged protons and uncharged neutrons held together by nuclear forces. Both protons and neutrons have approximately the same mass, which is about 1840 times as large as the mass of an electron [2]. Neutrons and protons are referred to collectively as nucleons. Spin is a fundamental property of

nuclear, which comes in multiples of 1/2 and can be + or -[3] .Nuclear spin is quantified by the nuclear gyromagnetic ratio(γ_N) and spin angular momentum vector(I). The gyromagnetic ratio is related to the magnetic moment vector (μ) and nuclear g factors(g_N). [4]

$$u = \gamma_N \hbar I = g_N \mu_N I \qquad \text{Equation 2-1}$$

Because nucleons have spin, just like electrons do, their spin can pair up when the orbitals are being filled and cancel out. Almost every element in the periodic table has an isotope with a non zero nuclear spin. NMR can only be performed on isotopes whose natural abundance is high enough to be detected. Since almost every nucleus has a unique gyromagnetic ratio(γ_N), it allows nuclei to be distinguished from one another spectroscopically. In this thesis, two isotopes of Li, ^{6}Li and ^{7}Li, were measured. The spin numbers and gyromagnetic ratios of these nuclei are summarized in Table 2.1. Also included is the spin number and gyromagnetic ratio of a free electron,

Nucleus	**γ(10^7rad/Ts)**	**abundance**	**I**
6Li	4	7.5%	1
7Li	10	92.5%	3/2

electron	1700

Table 2.1- spin numbers and gyromagnetic ratios for nuclei

$$\langle Sz \rangle = -\frac{B_0}{\mu_0 g N_0 \mu_B} \chi_M$$

Equation 2-2

Equation 2-2 shows the paramagnetic effects for nuclei in the magnetic field, while <Sz> is the time averaged spin density along +z-axis, this spin density is proportional to the molar magnetic susceptibility of the transition metal χ M, and the strength of the applied magnetic field. Therefore, low field has been used in our study to minimize the size of the paramagnetic interaction.

2.2 Spin Relaxation

2.2.1 Spin-Lattice Relaxation

When perturbed by the applied RF field. The system will return to thermal equilibrium by a process known as longitudinal or spin-lattice relaxation. At

equilibrium, the net magnetization vector lies along the direction of the applied magnetic field B_o and is called the equilibrium magnetization M_o. In this configuration, the Z component of magnetization M_Z equals M_o. M_Z is referred to as the longitudinal magnetization. There is no transverse (M_X or M_Y) magnetization here. It is possible to change the net magnetization by exposing the nuclear spin system to energy of a frequency equal to the energy difference between the spin states. If enough energy is put into the system, it is possible to saturate the spin system and make M_Z=0.

The time constant which describes how M_Z returns to its equilibrium value is called the spin lattice relaxation time (T_1). The equation governing this behavior as a function of the time t after its displacement is:

$$M_z = M_o (1 - e^{-t/T1}) \qquad \text{Equation 2-3}$$

If the net magnetization is placed along the -Z axis, it will gradually return to its equilibrium position along the +Z axis at a rate governed by T_1. The equation governing this behavior as a function of the time t after its displacement is:

$$M_z = M_o (1 - 2e^{-t/T1}) \qquad \text{Equation 2-4}$$

In summary, the spin-lattice relaxation time (T_1) is the time to reduce the difference between the longitudinal magnetization (M_Z) and its equilibrium value by a

factor of e. And the total relaxation is facilitated by a combination of the interactions with the local surroundings including, dipolar coupling, quadrupolar coupling, chemical shift anisotropy as well as spin-rotation

Measure T_1 by inversion-recovery method

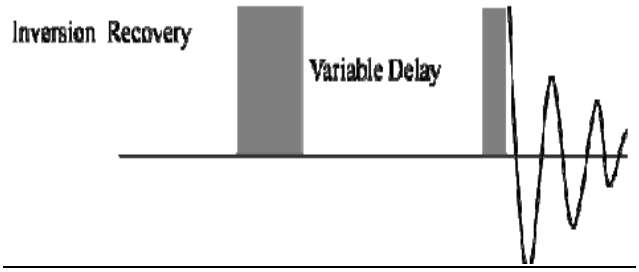

Figure 2.1-Pulse sequence for T_1 inversion-recovery method

Usually, T_1 values are measured using an inversion-recovery pulse sequence. Which means that a 180˚ pulse is applied to invert the magnetization, then a variable delay t, is given for the magnetization to relax. Finally, a 90 ˚ pulse is applied to measure the size of the magnetization that had relaxed along the z axis [5](Figure 2.1). By plotting the signal intensity, T_1 for each resonance can be measured.

2.2.2 Spin-Spin Relaxation

In addition to the rotation, the net magnetization starts to dephase because each of the spin packets making it up is experiencing a slightly different magnetic field and rotates at its own Larmor frequency. The longer the elapsed time, the greater the phase difference. Here the net magnetization vector is initially along +Y. The time constant which describes the return to equilibrium of the transverse magnetization, M_{XY}, is called the spin-spin relaxation time, T_2.

$$M_{XY} = M_{XYo}\, e^{-t/T2} \qquad \text{Equation 2-5}$$

T_2 is always less than or equal to T_1. The net magnetization in the XY plane goes to zero and then the longitudinal magnetization grows in until we have M_o along Z. Any transverse magnetization behaves the same way. The transverse component rotates about the direction of applied magnetization and dephases. T_1 governs the rate of recovery of the longitudinal magnetization.

In summary, the spin-spin relaxation time, T_2, is the time to reduce the transverse magnetization by a factor of e. Both T_1 and T_2 processes occur simultaneously with the only restriction being that T_2 is less than or equal to T_1.

Two factors contribute to the decay of transverse magnetization: molecular interactions and variations in B_o . The combination of these two factors is what actually results in the decay of transverse magnetization[6]. The combined time constant is called T_2 star and is given the symbol T_2*. The relationship between the T_2 from molecular processes and that from inhomogeneities in the magnetic field is as follows[7].

$$1/T_2^* = 1/T_2 + 1/T_{2inhomo}. \qquad \text{Equation 2-6}$$

The importance of T_2 relaxation time comes from its influence on the line-width of isotropic resonances of nuclear spins, which define as FWHM in this thesis. The FWHM of a peak is defined by $1/T_2$ which for paramagnetic systems(Equation 2-7), which was influence by both the hyperfine coupling as well as the spin-lattice relaxation of the electrons(T_{1e})[8]

$$FWHM = T_2^{-1} = T_{2N}^{-1} + (\frac{A_H}{\hbar})^2(\frac{T_{1e}}{8}) \qquad \text{Equation 2-7}$$

2.3 Lithium NMR Spectra of Cathode Materials

Since lithium ions are directly involved in the microscopic processes that take place in the batteries, lithium NMR plays an important role among the methods typically used to study battery materials [6]. The solid-state NMR techniques described in this thesis make it possible to probe the local environments surrounding the lithium ions. Furthermore, it gives us an opportunity to observe the dynamic process that is taken place during electrochemical cycling.

In Solid State NMR, the main three interactions that lead to very broad peaks are dipole-dipole interactions (Chapter 2.4.2), chemical shift anisotropy and a quadrupolar interaction. For this reason, we use Magic Angle Spinning (MAS) to average these three time-dependent interactions. The nuclear dipole-dipole interaction between magnetic moments of nuclei averages to zero only at the magic angle, θ_m. The chemical shift anisotropy, a nuclear-electron interaction, averages to a non-zero value. The quadrupolar interaction is only partially averaged by MAS leaving a residual secondary quadrupolar interaction. By spinning the sample at the magic angle θ_m (ca. 54.74°, where $\cos^2\theta_m=1/3$) with respect to the direction of the magnetic field(Figure 2.2), the normally broad lines become narrower, increasing the resolution for better identification and analysis of the spectrum. Also, by spinning at different magic angle spinning speeds may help distinguish the isotropic peak from spinning

sidebands.

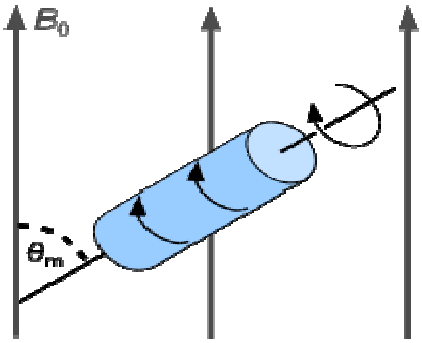

Figure 2.2-sample by Magic Angle Spinning

Due to the unpaired electrons sitting on the transition metal center of the paramagnetic materials, NMR of paramagnetic materials become significantly different compare to diamagnetic materials. In general, the main interaction in paramagnetic system which causes line broadening and low resolution are strong paramagnetic effect, dipole interaction and Chemical Shielding Anisotropy(CSA). And the effect of these interactions can be minimized and spectra simplified by using low fields, fast MAS, and nuclei with low γ s(Equation 2-2) [9].

2.4 NMR of Paramagnetic Cathode Materials

2.4.1 Fermi-Contact Interaction

Equation 2-8 shows the Fermi-contact Hamiltonian, where s_i stands for the ith electron spin and I means the nuclear spin, the vector r_i stands for the geometry dependence between them.

$$H_F = \frac{16\pi\hbar\gamma_N\beta}{3}\sum_i \delta(r_i)s_i \cdot I \qquad \text{Equation 2-8}$$

In this thesis, the geometry dependent mechanism of the coupling follow the Goodenough-Kanamori rules, these rules describe spin-spin super exchange, which is between the unpaired electron spin density on transition metal center and the nuclear spin on Li in materials studied here. The transition metal centers of materials studied here all have octahedral coordination, which leads to a split of d-orbital into t_{2g} and e_g states. t_{2g} is a triply degenerate state including orbitals d_{xy}, d_{yz}, d_{xz} while e_g is a doubly degenerate state with higher energy including orbitals $d_{x^2-y^2}$ and d_{x^2}. There are two mechanisms applied to described the geometry of the spin transfer shown here - the delocalization mechanism and the polarization mechanism. The polarization mechanism(shown in Figure 2.3) [9], will lead to a decrease in the Li-atom chemical shift, because the electron spin density of the t_{2g} orbital is polarized by unpaired

electrons in the e_g orbital of the transition metal, which increases the positive spin density of transition metal center thus leading to negative spin density on the O 2p orbital, which is then transferred to the Li 2s orbital. This results in net transfer of negative spin polarization from transition metal center to the empty 2s Li orbital, which results in a negative shift. However, this transfer has a significant effect only when the M-O-Li (M = transition metal) orbitals overlap at angles close to 180 degree, which is not found in materials studied in this thesis. The delocalization mechanism (shown in figure 2.3) will transfer the unpaired electron spin density from the t_{2g} orbital of the transition metal to the empty Li 2s orbital through the O 2p orbital, which leads to an increase of the Li atom chemical shift. This transfer is effective only when the M-O-Li orbital overlap at an angle close to 90˚ (Figure 2.3).

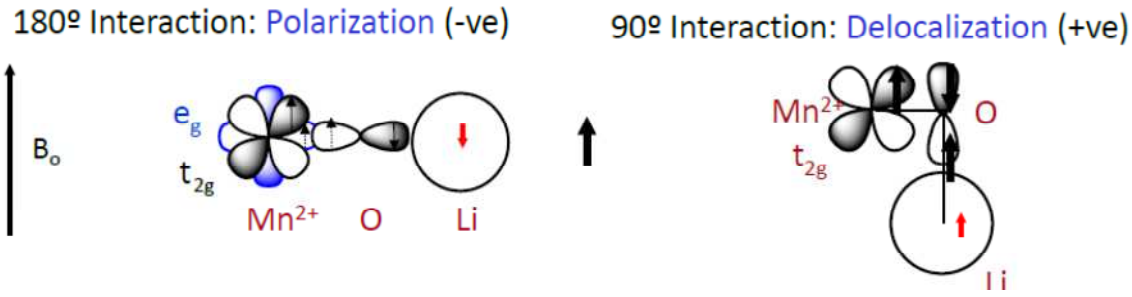

Figure 2.3- Polarization and Delocalization mechanism

2.4.2 Dipolar Coupling

Dipolar coupling is an interaction that can occur between both homonuclear and heteronuclear spin pairs. It is caused by the local magnetic fields of the nuclear or electronic (S) spins that are felt at the nearby nuclear (I) spin[10]. Equation 2-9 shows the simplified dipolar Hamiltonian(H_D). When only considering the dipolar coupling between (j, k) spin pairs, the dipolar interaction just related to gyromagnetic ratio of both spins and the internuclear distance r_{jk}

$$H_D = \frac{\mu_o}{4\pi}\frac{\gamma_j\gamma_k\hbar}{r_{jk}^3}(3\cos^2\theta - 1)\frac{(3I_{jz}I_{kz} - \hat{I}_j\hat{I}_k)}{2} \qquad \text{Equation 2-9}$$

As it mentioned previously, by spinning the sample at the magic angle θm (ca. 54.74°, where $\cos 2\theta_m = 1/3$) with respect to the direction of the magnetic field, time-dependent both interaction and CSA can be averaged to 0. The normally broad lines become narrower, increasing the resolution for better identification and analysis of the spectrum. However, the size of the dipolar interaction (Equation 2-10) and CSA contribution are generally larger than the MAS frequency, a series of spinning sidebands result in the spectrum. Thus, the line broadening is no longer completely removed by MAS. More detailed studies are still, however, required to correlate this interaction with line broadening.

$$Dij = \frac{\mu_0 \gamma_i \gamma_j}{4\pi r_{ij}^3}$$ Equation 2-10

It was shown in Table 2-1 that gyromagnetic ratio values of an electron spin is significantly larger than the gyromagnetic ratio of the nuclear spins studied in this thesis(^{6,7}Li). This indicates that the effect of nuclear-electron coupling is much greater than homonuclear or heteronuclear couplings. The strong dipole interaction makes paramagnetic materials especially challenging to study

2.5 One-Dimensional Selective Inversion Experiment

2.5.1 Introduction to other SSNMR techniques used in dynamic study

This section outlines the general NMR techniques that have previously been used to characterize dynamics of cathode materials.

Rotational-echo, double-resonance(REDOR) experiments are used to measure

the heteronuclear dipolar couplings. The basis of the REDOR experiment is the measurement of spectral signal intensity before and after the perturbation of a dipolar coupled heteronuclear partner. REDOR experiments probe the relative internuclear distance between a heteronuclear spin pair, correlating the Li ions to atoms in the host framework. REDOR has been used to mearure Li ion dynamics in $LiFePO_4$ in previous work done by our group, since changes to the Li-P dipolar couplings are attribute to mobility of the Li ion within the framework.

Two-dimensional exchange spectroscopy (2D EXSY) are applied for identify and quantify ion-hopping pairs. Two dimensional NMR measurements were first introduced by Kumar et al.[10]. To determine the timescales of chemical exchange from 2D EXSY measurements in systems undergoing ion exchange, the mixing time is stepped over a series of experiments and the volume of the cross peak measured . An exponential buildup of cross peak integration as a function of mixing time is fit to yield a correlation time of the exchange process. An Arrhenius analysis of the inverse correlation times over a variable temperature range produces the energy barrier.

2.5.2 Introduction of One-Dimensional Selective Inversion Experiment

To characterize the structure and dynamic of cathode material presented in Chapter 1, a series of NMR experiments have been applied in this thesis. Application of these experiments over a variable time and temperature range identifies Li ion hopping pairs and subsequent determination of timescales and energy barriers. This work is complemented by one-dimensional selective inversion studies, which is a simpler mean to probe ion dynamic compare to 2D EXSY studies and require considerably smaller amounts of spectrometer time. Overall, the determined ion-hopping timescales are compared between the materials presented in Chapter 1 where a set of structural parameters observed to enhance on inhibit ion mobility are considered.

Selective Inversion methods are 1D relaxation-type experiments, which monitor the effect of chemical exchange on the magnetization's return to equilibrium[11]. This experiment selectively inverts a spin undergoing ion exchange, this spin can then return to equilibrium by exchange with the non-inverted sites (Figure 2.4). By monitoring the return to equilibrium as a function of mixing time (τ_{mix}), mobility timescales can be determined for cathode materials. It provides a good way to measure dynamic process in material which Li^+ ions exchange slowly relative to their T_1 spin-lattice relaxation[12]. On the other hand, It is less difficult and more time efficient to obtain good quantitative data with 1D techniques compare to 2D-EXSY

experiments. The goal of this thesis is to apply more time and cost effective methods for determining timescales of ion mobility where the short T_1 and T_2 times placed fewer limitations on the data analysis. This lead to the use of 1D ^{6,7}Li selective inversion experiments as a mean to expand the determination of ion-hopping timescales to more slowly exchanging materials. In the 1D measurement, the relaxation of a selectively inverted spin is monitored as function of both the inherent T_1 properties as well as the exchange processes taking place with non-inverted spin(s). The return to equilibrium of the inverted site is measured as a function of mixing time(τ_{mix}). In a multi-spin system, the relaxation of the inverted spin has combined effects of inherent spin-lattice(T_1) relaxation time as well as the rate constants(k) associated with each exchange process taking place with the measured spin.(Equation 2-11)

$$R_i = \frac{1}{T_{1i}} + \sum_{i \neq j} k_{ij}$$

Equation 2-11

The initial inversion step is followed by a mixing period where the chemical exchange processes take place. A series of 1D experiments are measured over a function of mixing time for both the inverted and non-inverted sites. In this thesis, shaped pulse selective inversion is applied for measurement of timescales and energy

barriers of ion hopping in a series of materials.

The dataset collected by selective inversion experiment is then fit in a program called CIFIT to yield accurate exchange timescales. CIFIT is a C program based on McClung's SIFIT (Selective Inversion FIT) and is introduced in next section[13].

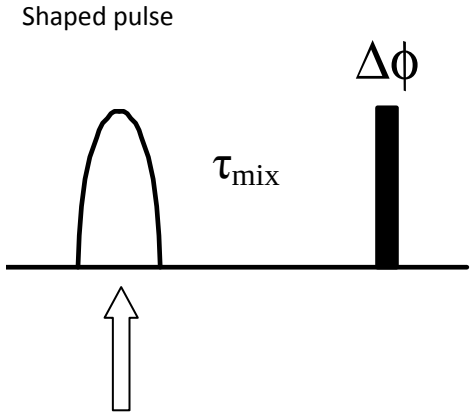

Figure 2.4-Pulse sequence for shaped pulse selective inversion experiment

2.5.2 CIFIT Used for Data Fit

CIFIT is a C based program used for data analysis for selective inversion data set. What CIFIT needs for data analysis are: Initial magnetization values, spin relaxation time for each resonance and a table of observed intensities for all spins as a function of mixing time. CIFIT can then determines a key set of parameters: the jump rate (k) of each chemical exchange process, spin-lattice relaxation times in the absence of chemical exchange (T_1), and the magnetization values from initial to equilibrium conditions (i.e. from Mi(0) to Mi(*) The primary mathematical model used by the CIFIT program is a rate matrix describing the relaxation of magnetization for a system with n sites(Equation 2-12)

$$\begin{pmatrix} \mathrm{M}_A(\infty) - M_A(t) \\ \vdots \\ \mathrm{M}_B(\infty) - M_B(t) \end{pmatrix} = \exp(A_{AB}t) \begin{pmatrix} \mathrm{M}_A(\infty) - M_A(0) \\ \vdots \\ \mathrm{M}_B(\infty) - M_B(0) \end{pmatrix} \qquad \text{Equation 2-12}$$

Where

$$A = \begin{pmatrix} R_{11} - k_{21} - k_{31} \cdots - k_{n1} \\ -k_{12} R_{22} - k_{32} \cdots - k_{n2} \\ -k_{13} - k_{21} R_{33} \cdots - k_{n3} \\ \vdots \\ -k_{1n} - k_{2n} - k_{3n} \cdots R_{nn} \end{pmatrix}$$

Equation 2-13

k_{ij} stands for the exchange rate constant for the forward hop from i to j, and the relaxation(R_{nn}) is defined as the T_1 of the nth spin plus the sum of the rates for each exchange process in which that spin participates.

When the concentrations of the two spins are equal (which means the Li sites are fully occupied in cathode materials in our study) and the system has reached equilibrium, the rates of the forward and reverse processes are equal. The rate constants (k_{ij} and k_{ji}), therefore, will be equal as well. It is now more convenient to evaluate the exchange process from the standpoint of the equilibrium constant (K) rather than the rate constants themselves. The solution to the exchange matrix can then be written where T_1 relaxation is now ignored and the rate is fit as a single parameter

Therefore, what CIFIT does is applying this mathematical model until the sum of the squares of the differences between the experimental and modeled data is minimized.

2.5.3 Shaped Pulse Selective Inversion Experiments

In this thesis, shaped pulse selective inversion experiment is applied for measurement, which uses a Gaussian Shaped Pulse (SP) that placed on resonance to a site chosen for selective inversion. This method is suitable to study materials that have multi-exchange pairs and is therefore used to study ion hopping timescales in $Li_2MnP_2O_7$.

The Gaussian Shaped Pulse applied here is a long, soft, Gaussian shaped pulse, which ensures the inversion of only one sites that undergoing ion exchange, and leaving all other sites unperturbed. This experimental approach will be referred to as the shaped pulse method. A drawback to this method is that the shaped pulse can become very long (500us to 1ms) for the desired bandwidth to be reached. In paramagnetic systems these lengths are on the order of the relaxation time of the spin-chosen for inversion, and competition between complete inversion and relaxation results.

2.6 Summary

This chapter outlines the basic principle NMR and details the NMR experiments used in this thesis to study the structural and dynamic process for cathode materials.

2.7 References

(1) Tarascon, J.M. and M. Armand, Nature, 2001. 414(6861): p. 359-367.

(2)Carrington, A.;Mclachlan, A.D, Introduction to Magnetic Resonance: NewYork, 1967.

(3)Levitt,M.H. Spin dynamics:Basic of Nuclear Magnetic Resonance:West Sussex, 2001.

(4)Duer,M.J. Introduction to Solid-State NMR Spectroscopy: Oxford, 2004.

(5) Zaghib, K., et al., Journal of Power Sources, 2006. 160(2): p. 1381-1386.

(6) Nagaura, T.; Tozawa, K. Prog. Batteries Solar Cells 1990: p.209

(7)La Mar, G.N., DeW.Horrocks, W.,Jr., Holm, R.H. NMR of Paramagnetic Materials; New York, 1973

(8) Grey, C.P. and N. Dupre, Chemical Reviews, 2004. 104(10): p. 4493-4512.

(9)Davis,L.J.M., I.Heinmaa, and G.R.Goward, Phys.Chem.Chem.Phys, 2010. 10: p.1039-1042

(10) Adam, L., A. Guesdon, and B. Raveau, Journal of Solid State Chemistry, 2008. 181(11): p. 3110-3115.

(11) Forsen, s.; Hoffman, R. A. J. Chem. Phys. 1963, 39, 2892

(12) Forsen, s.; Hoffman, R. A. J. Chem. Phys. 1964, 40, 1189

(13) Bain,A. D.; Fletcher, D.A.Mol. Phys. 1998, 95, 1091

Chapter 3: Structure Information and Quantification of Li Ion Mobility of $Li_2MnP_2O_7$ Using ^{6,7}Li MAS Measurement

3.1 Introduction

In this chapter, ^{6,7}Li MAS NMR measurement are used to characterize Li environments in $Li_2MnP_2O_7$, ^{6}Li 1D Selective inversion(SI) measurements were done at a series of temperatures to quantify the timescales of ion hopping in the $Li_2MnP_2O_7$.

The $Li_2MnP_2O_7$ was first reported by Adam.et.al. [1] It has a 3D framework built up of manganese polyhedra and phosphate tetrahedra(Figure 3.1) [2]. In the structure, MnO_5 is sharing an edge with MnO_6, which forms Mn_2O_9, and each Mn_2O_9 is then connected with P_2O_7 groups. [1] Here we use ^{6,7}Li MAS NMR to investigate the Li environments in this material.

The lithium cations have various coordinations, as is shown in Figure 3.1.1. Li1 and Li2, which sit in the six-sided tunnels, exhibit a distorted square tetrahedral coordination, respectively. The Li–O distances are comprised between 1.98 and 2.35A˚ in the Li1 pyramids, and between 1.90 and 2.00A˚ in the Li2 tetrahedra. Li3 and Li4, which sit in the five-sided tunnels, exhibit a distorted tetrahedral coordination, The Li3 tetrahedra are indeed very distorted with Li–O distances ranging from1.89 to 2.29A˚, whereas in the Li4, Li–O distances ranging from1.96 to

2.33A˚.

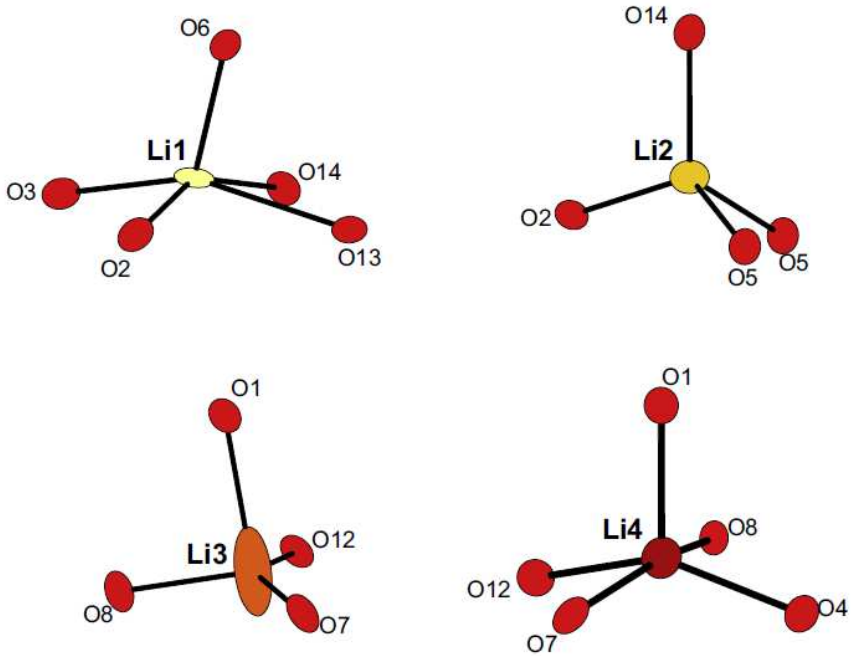

Figure 3.1-Environment of the lithium cations in $Li_2MnP_2O_7$

Thermo gravimetric analysis and magnetic tests confirm the 2+ oxidation state for the $Li_2MnP_2O_7$. However, the electrochemistry is proved to be very poor according to Zhou.et.al[3]: it has low capacity, high polarization, and no voltage plateau during charge or discharge. To check whether the extraction of the second lithium ion is possible, the cyclic voltammetry for $Li_2MnP_2O_7$ was performed with an extended voltage range of 1.5-5.5 V, and clearly oxidation peak at a high potential of 5.3 V is observed, which might be due to the Mn^{3+}/Mn^{4+} redox couple. For $Li_2MnP_2O_7$,

although no experimental voltage profile is obtained, because of its very poor capacity, good agreement with the cyclic voltammetry is found: two oxidation peaks are observed, at 4.5 V and 5.3 V. Unlike $Li_2MnP_2O_7$, $Li_2FeP_2O_7$ shows much better electrochemical performance than the Mn phase. [4]

In this thesis, we aim to understand the ion dynamic in the $Li_2MnP_2O_7$, using variable temperature ^6Li MAS measurement. Under the current experimental temperature range(230K-340K), peak coalesence was observed around 330K which suggested that ion dynamic process do exist in this material.(Figure 3.7).

The thesis also introduces the use of one-dimensional selective inversion methods to determine the ion hopping rates in the $Li_2MnP_2O_7$. 1D selective inversion experiments monitor the return of magnetization to equilibrium conditions following the selective inversion of a slow-dynamic system. [3] The ion relaxation is governed not only by the inherent spin-lattice relaxation of the nuclei, but also by the rate of ion exchange with non-inverted spins. A series of data sets at variable temperature were obtained by shape pulsed selective inversion experiments, and these data sets were then fit using the CIFIT program, which was able to separate the ion exchange timescales from inherent T_1 properties. Compared to traditional 2D method for ion dynamic measurement, these 1D experiments are more efficient in terms of spectrometer time. Moreover, this method reveals timescales of ion hopping in

materials where the Li ions exchange slowly relative to their T_1 spin-lattice relaxation. This situation is particularly relevant to cathode materials for lithium ion batteries, where the unpaired electrons of the transition metal centers provide a dominant mechanism for rapid relaxation. Therefore, the introduction of this 1D selective inversion methods give us an opportunity to quantify ion hopping timescales in a larger range of materials that were previously excluded due to these T_1 limitations.

3.2 Experimental

3.2.1 Sample Preparation

A pure phase $Li_2MnP_2O_7$ sample was synthesized using a convenient solid-state reaction [1] in two steps, starting from a mixture of MnO, Li_2CO_3 and $(NH_4)_2HPO_4$. The mixture was ground for 30 min then heated in air at 600°C for 2 hours (5 hours from room temperature to 600°C) and reground. Then the precursor was transferred into an evacuated silica tube, which was heated at 650°C for 15h, after which the product was cooled to 550°C at a rate of 2 °C/h, before being brought back to room temperature. After first step, the product obtained after grounded turns to grey, (XRD pattern in Figure 3.2,top) and the final product $Li_2MnP_2O_7$ is pink. (XRD pattern in Figure 3.2,bottom). After the compare of XRD pattern to the calculated XRD pattern

of MnO and MnO_2, it indicates that there is no remaining MnO after first step, while there is some MnO_2 formed, and the product after first step is a mixed phase sample.

Zhou et.al has reported another synthesis route for this material named “wet” method. The procedure involves the mixing of soluble precursors: $Li(CH_3COO)$, $Mn(CH_3COO)_2$, and $NH_4H_2PO_4$, which are dissolved in 100mL of distilled water to give a 0.02M lithium solution. The pH values are determined to be 4.5-5. The solutions are evaporated then followed by vacuum oven overnight drying at 90˚C. Finally, the solids are annealed in a H_2/He atmosphere at temperatures ranging from 400˚C to 700˚C with intermediate grinding.

3.2.2 Powder XRD

An x-ray diffraction (XRD) pattern of the synthesized sample was obtained using a PANalytical diffractometer from 2θ= 10-60˚ with Cu Kα radiation at 45kV and 35mA. The count rate is 1 sec per step of 0.02˚. The reflections were using DICVOL91 software.

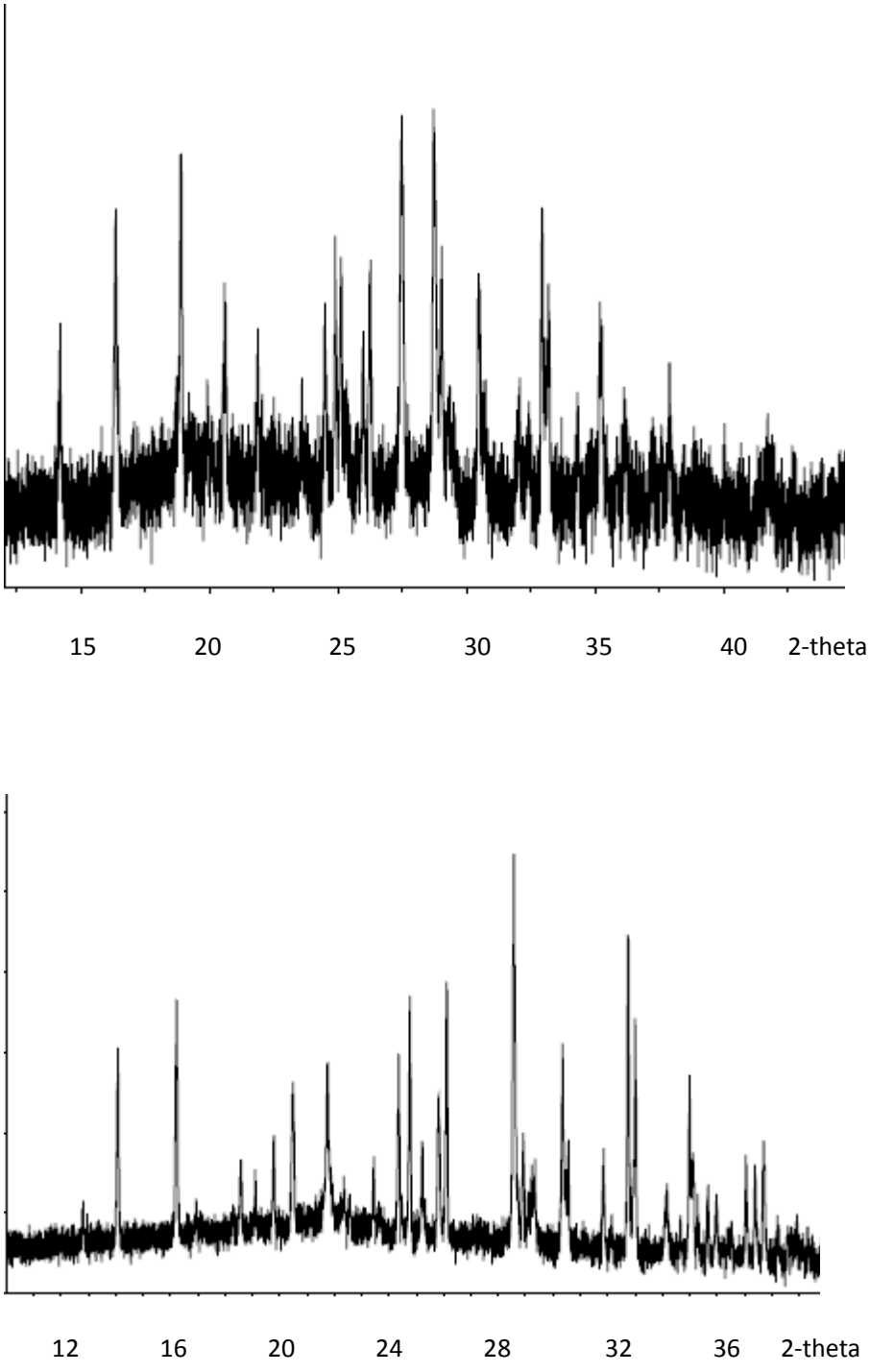

Figure 3.2-XRD pattern of product after first step (top) and XRD pattern of $Li_2MnP_2O_7$ (bottom)

3.2.3 Solid-State NMR

NMR measurements for $Li_2MnP_2O_7$ samples were performed on a Bruker AV-300 spectrometer using a custom made 1.8 mm probe at Larmor frequencies of 116.6 MHz for ^{7}Li, and 44.2 MHz for ^{6}Li. All ^{6,7}Li shifts were reference to 1M ^{6,7}LiCl (0 ppm). Measurements carried out here include room temperature 1D ^{7}Li MAS measurements of each sample. ^{6,7}Li 1D spectrum were obtained using a Hahn-echo pulse sequence(90° – τ - 180°) with 90° pulses at 3.5 μs and recycle delays range from 0.1-0.2s. Spin lattice relaxation times(T_1) were obtained using standard inversion recovery sequence.

Variable temperature ^{6}Li MAS measurements were carried out on a custom built 1.8mm probe. The temperature range from 230K to 350K. Both variable temperature study and 1D selective inversion experiments were measured over this temperature range.

1D ^{6}Li selective inversion experiments were also performed on a Bruker AV300 spectrometer with supporting 1.8mm rotors. 1D selective inversion experiments were performed using a 180- τ mix-90, where the 180 pulse was a long, Gaussian pulse, which has been applied to the resonance chosen for inversion [6], 90° pulse was calibrate to 3.5μs, recycle delay of 200ms, and 10240 scans were used for each slice.

The total experiment time at one temperature is around 16 hours. Mixing times were stepped over a series of 16 experiments from 5μs to 100ms. Nonselective inversion(NSI) experiments were performed using the standard inversion-recovery sequence. [7] The same variable delay list was used in the NSI experiments. In all these experiments, a digital filter was applied to allow for acquisition.

All spectrum were referenced to 1M LiCl(aq) (0ppm). Temperatures were calibrated using $Sm_2Sn_2O_7$. [8]

3.2.4 1D Selective Inversion Data Analysis

In each data set, slices for each mixing time were extracted and baseline corrected. After integrating both spins involved in the exchange process, these values were normalized to the integration value of the slice collected at the longest mixing time. The data was fit using the CIFIT program developed by A.D.Bain[9]. This program uses a table of observed intensities for all spins as a function of mixing time and determines a key set of parameters: the jump rates(k) of each chemical exchange process, spin-lattice relaxation times in the absence of chemical exchange(T_1), and the magnetization values from initial to equilibrium conditions(Mi(0) to Mi(∞)), CIFIT adjusts the free parameters, T_1, k, Mi(0) and Mi(∞), using a Levenberg-Marquart

algorithm until the sum of the squares of the differences between the experimental and calculated data is minimized

3.3 Result and Discussion

3.3.1 ^{6,7}Li MAS NMR of $Li_2MnP_2O_7$

The 1D ^{7}Li spectrum for $Li_2MnP_2O_7$ is shown in Figure 3.3. At fast magic angle spinning(MAS= 40 kHz) , three peaks were resolved in the ^{7}Li MAS NMR spectrum collected at 300K with isotropic shift around 0ppm. T_1 measurements show short spin-lattice relaxation time (T_1) of each resonance(around 1ms), which indicates the strong paramagnetic effect for Li-resonance.

The 1D ^{6}Li spectrum for $Li_2MnP_2O_7$ is shown in Figure 3.3. Higher resolution is obtained, and a small shoulder around 0ppm is observed, which indicated 4 crystallographic sites for $Li_2MnP_2O_7$. This is in agreement with the Rietveld refinement XRD results performed by Adam.et.al and Hui.et.al. [1][2] They refined the splitting of the Li site in $Li_2MnP_2O_7$ as a Li1 : Li2 : Li3 : Li4 occupancy of 1 : 1 : 1 : 0.4. Our NMR results deconvoluted throughout the full spinning sidebands manifold appears to have similar values .

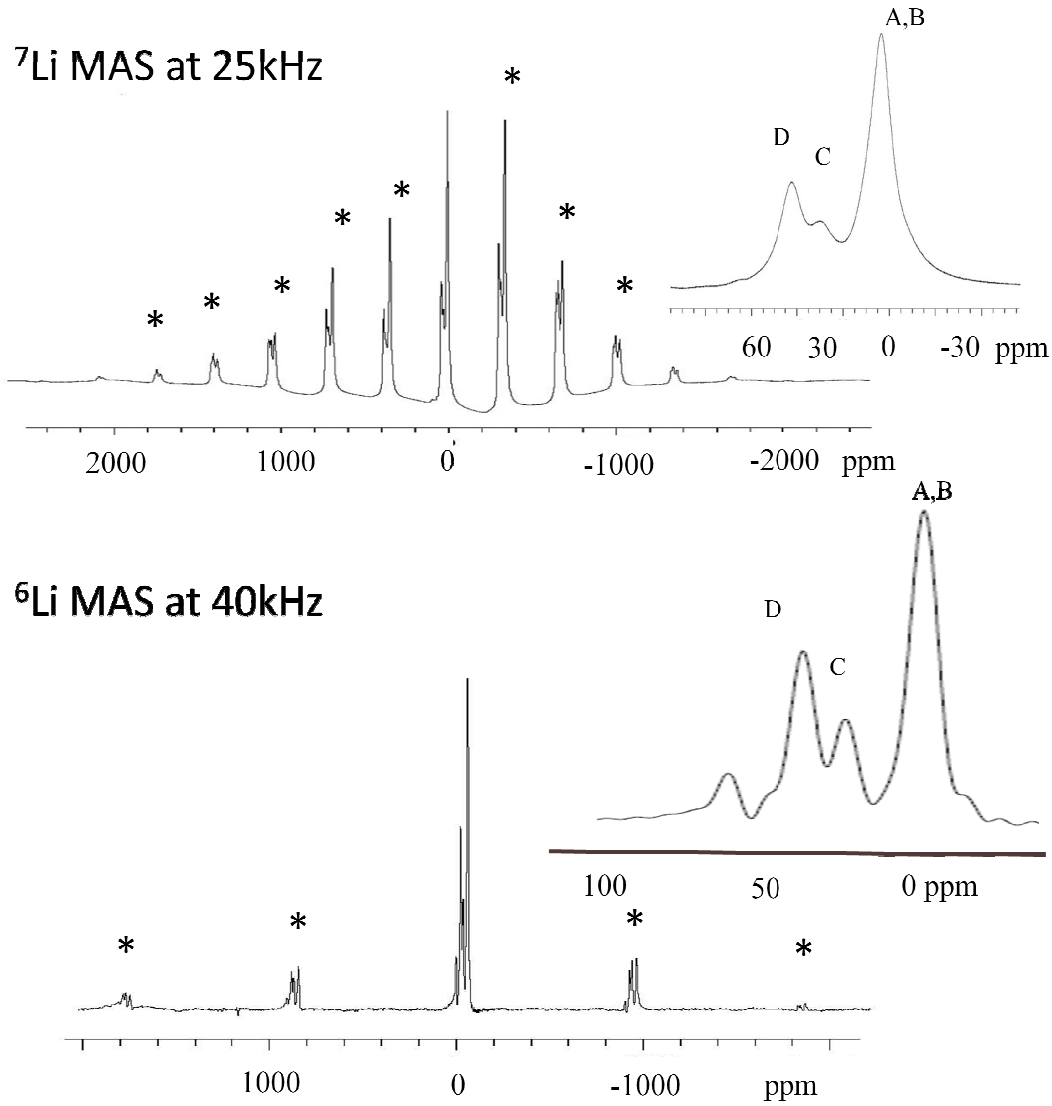

Figure 3.3-^{6}Li and ^{7}Li MAS spectra of $Li_2MnP_2O_7$, * refer to spinning sidebands.

3.3.2 Site Assignment of $Li_2MnP_2O_7$

The deconvolution of the isotropic peak is shown in Figure 3.4, enabling us to

see four crystallographic lithium positions in the spectrum. The assignment of each resonance to the crystallographic positions was made in reference to some previous work[7], which was based on measuring the amount of electron spin density which was transferred from the paramagnetic transition metal center to Li atoms. There are two mechanisms for electron spin density transfer:the delocalization mechanism and the polarization mechanism. The polarization mechanism(shown in Figure 3.5) [8], will lead to a decrease in the Li-atom chemical shift, because the electron spin density of the t_{2g} orbital is polarized by unpaired electrons in the e_g orbital of the transition metal, which increases the positive spin density of transition metal center thus leading to negative spin density on the O 2p orbital, which is then transferred to the Li 2s orbital. However, this transfer has a significant effect only when the M-O-Li (M = transition metal) orbitals overlap at angles close to 180 degree, which is not found in our crystal structure. Therefore we do not need to take the polarization mechanism into consideration when we try to do the assignment.The delocalization mechanism (shown in Figure 3.5) will transfer the unpaired electron spin density from the t_{2g} orbital of the transition metal to the empty Li 2s orbital through the O 2p orbital, which leads to an increase of the Li atom chemical shift. This transfer is effective only when the M-O-Li orbital overlap at an angle close to 90 degrees(Figure 3.5). We make the assignment mainly based on the delocalization mechanism. The Mn^{2+} has an

electron configuration of $t_{2g}^3e_g^2$.

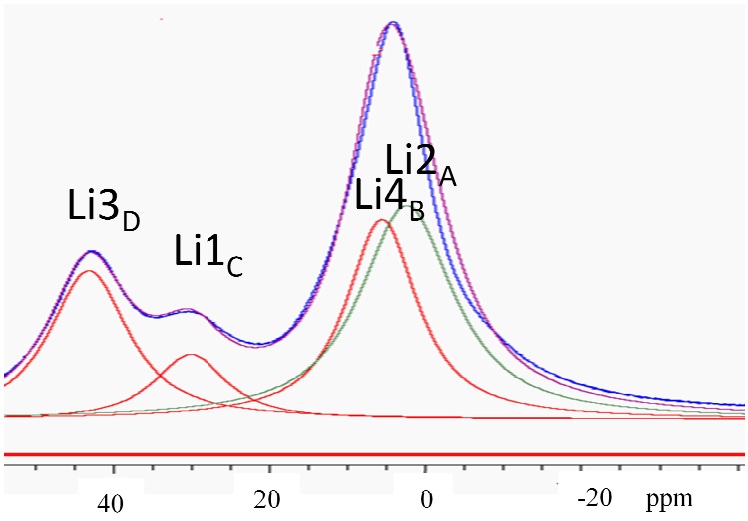

Figure 3.4- Deconvolution for ^{7}Li MAS spectra of $Li_2MnP_2O_7$

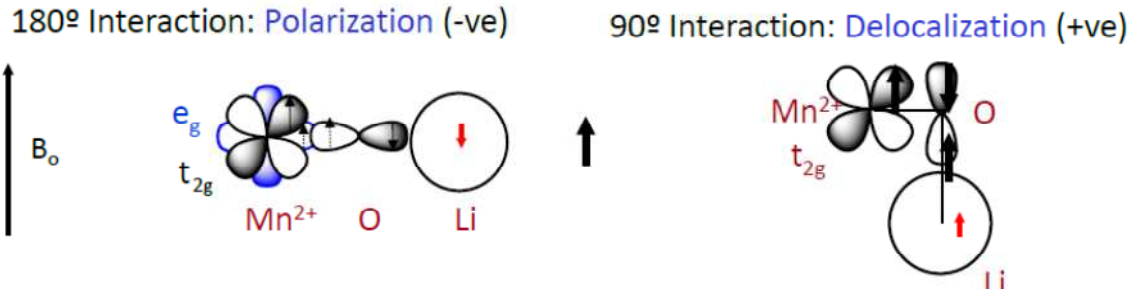

Figure 3.5- Polarization and Delocalization mechanism

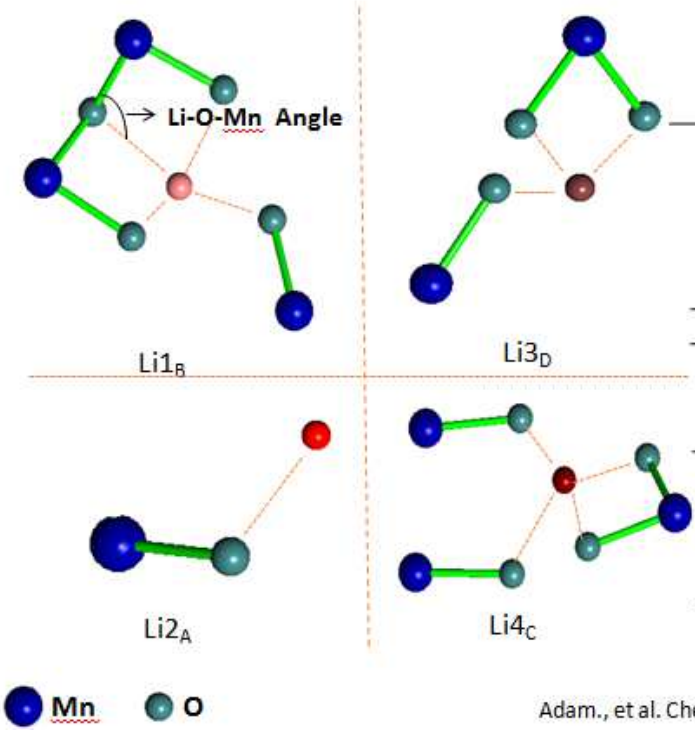

Li site	Li-O-Mn Angles (deg)	Li-Mn Distance (Å)	Li-O Distance (Å)
1	**94.35**	**3.353**	**2.325**
	96.07	3.353	2.093
	88.33	**3.173**	**2.325**
	99.28	3.173	1.988
	110.89	3.467	2.354
2	105.66	3.309	2.152
3	111.65	3.697	1.999
	94.25	**3.010**	**1.966**
	89.53	**3.010**	**1.951**
4	116.77	3.548	2.229
	119.26	3.915	1.985
	90.87	**3.175**	**2.333**
	100.37	3.175	1.969

Adam., et al. Chemistry of Materials, 2008. **23**(2): p. 293-300.

Figure 3.6-(left)Lithium coordination environments in $Li_2MnP_2O_7$. The Mn centers depicted are found in the second coordination sphere and are responsible for transfer positive spin density to the Li nucleus. The lithium atoms are shown in different red, oxygen atoms in grey, and Mn in blue. (right)Crystal structure data of $Li_2MnP_2O_7$

Therefore, the Li site with largest number of Li-O-Mn angles close to 90° will have the highest chemical shift, while the Li site with the poorest Li-O-Mn overlap should have the lowest chemical shift[9]. One more thing to pay attention to when we consider the transfer of electron spin density through the Li-O-Mn bond, is that the Li-O distance will also have an effect. In general, if the Li-O distance is significantly

greater than 2.0A, very little electron spin density can be transferred. So a bond length less than 2.3A is also needed for electron spin density transfer[10].

Taking all those into consideration, together with the crystallographic data of $Li_2MnP_2O_7$ (Figure 3.6), $Li3_D$ sites have highest frequency, $Li1_{C,}$ $Li4_B$ site lower, $Li2_A$ site the lowest (poorest Li-O-Mn overlap)

3.3.3 1D Variable Temperature Measurements

In order to confirm whether there is any dynamic process taking place in this material, variable temperature studies have been applied. Figure 3.7 shows a one-dimensional (1D) variable-temperature study from 230 to 330 K, with the sample temperature corrected to include the heating effects of spinning at 25 kHz. The chemical shift has a linear dependence on temperature, showing Curie-Weiss behavior [11]

It also appears that A and B resonance begin to coalesce at around 300K, meaning that at this temperature these two sites are exchanging at a rate of $\pi\nu/\sqrt{2}$ comparable to the separation in 900Hz between the two resonances(Table 3.1)[12]. Since we have already identify two possible exchange pair according to the crystal

structure data(Figure 3.6), combine with the analysis of assignment we discussed above, we can confirm that our assignment of $Li_2MnP_2O_7$ before is reasonable.

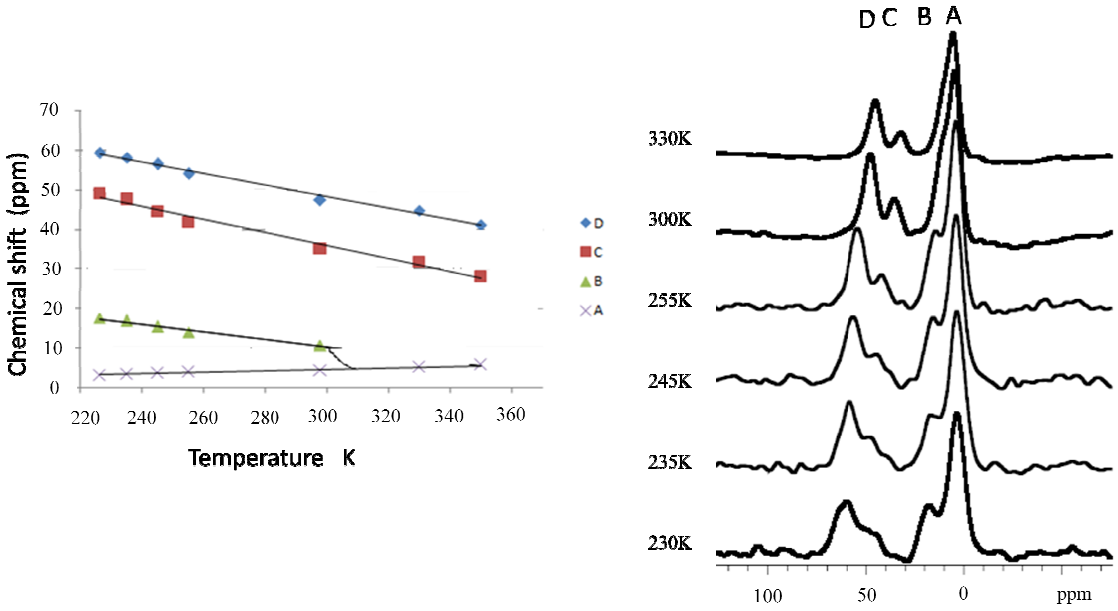

Figure 3.7- (left)Plot of chemical shift to temperature for each resonance (right)^{6}Li MAS spectrum obtained at VT

	Coalescence temp(K)	Jump frequency(kHz)	Correlation time(m
AB	300-305	900±30	1.1±0.2

Table 3.1- Jump frequency and correlation time for AB exchange pair.

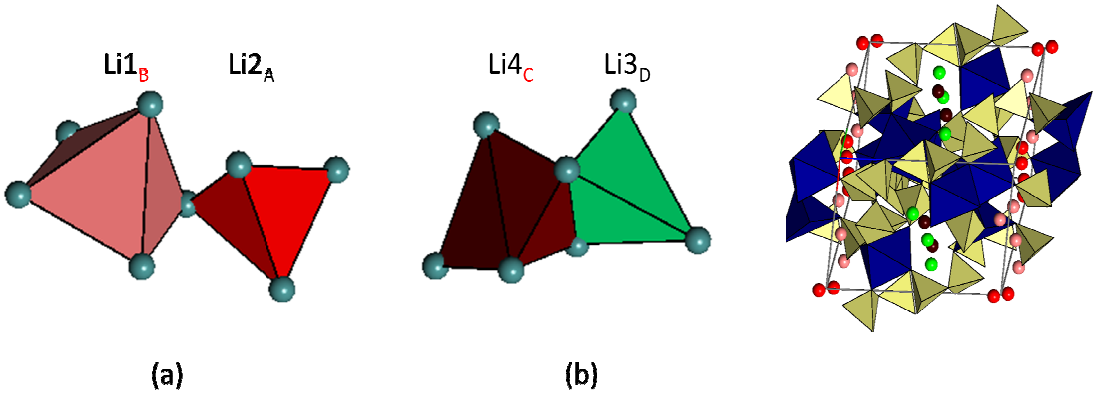

Figure 3.8- Two identified exchange pair from crystal structure data(left) and crystal structure of $Li_2MnP_2O_7$(right)

NMR Site	Li Site	Li-Li distance(Å)
BA	Li1-Li2	3.073
BD	Li1-Li3	4.213
BC	Li1-Li4	5.078
AD	Li2-Li3	4.787
AC	Li2-Li4	6.012
DC	Li3-Li4	2.972

Table 3.2- Summary of Li environments in $Li_2MnP_2O_7$

3.3.4 Quantification of Ion Dynamics in $Li_2MnP_2O_7$ using ^6Li 1D Shaped Pulse Selective Inversion Experiments

Since slow dynamic has been observed in the above variable temperature study for this material, 1D selective inversion experiments have been applied for dynamic study, and shaped pulse experiments were used in this thesis. These experiments used a 180- τ mix-90, where the 180 pulse was a long, Gaussian pulse, which has been applied to the resonance chosen for inversion[13]. A series of pulse length have been applied to set the different initial condition of the experiments. At each pulse length, power level has been calibrate to get the maximum inversion of the on-resonance resonance. Both Non-selective inversion and selective inversion experiments are using the same series of mixing time(τ mix) range from 5us to 100ms. Non-selective inversion(NSI) recovery experiments used a standard inversion-recovery sequence with the variable delay list set equivalent to the variable mixing time list of the Shape pulsed experiments. [14]

Figure 3.3 shows the ^6Li MAS spectra of $Li_2MnP_2O_7$, It should be a 4-site material according to the crystal structure data[15]. As we see in the spectra, the paramagnetic shifts arising at 4ppm, 21ppm, 41ppm, 60ppm, were labeled as A B C D,

respectively. After data acquired by shaped pulse selective inversion experiments, CIFIT is used for data analysis. As mentioned in previous chapter(2.1.3), CIFIT is able to fit these data sets to get the ion exchange timescales. In general, as a 4-site material, $Li_2MnP_2O_7$ should have 6-possible exchange pair, but structure analysis**(**Table 3.2) indicates that only two exchange pairs are possible here(Figure 3.8) [16], because except for Li1-Li2, Li3-Li4 these two pairs, the distance between other pairs of Li is too far. The timescales and energy barriers in the 4-site 6-possible-exchange model compound, $Li_2MnP_2O_7$, were measured using shape pulsed experiments over a variable temperature range(260K-350K). The CIFIT parameters were set such that six rates of ion-exchange: k_{ab}, k_{ac}, k_{bc}, k_{ad}, k_{bd}, k_{cd}. were determine for the exchange pairs. A-B, A-C, B-C, A-D, B-C, C-D, respectively. However, after multiple attempts trying to fit those data sets in CIFIT(Table 3.3), it finally turns out that kac, kbc, kad, kbd should be set to zero. Those setting was also confirmed by the crystal structural analysis, which indicates only two exchange pairs were exists in this material. The results for inversion of D, over a variable temperature range are shown in Figure 3.10. For all temperatures, there is a clear increase trend observed with the increase of temperature.

Input rate(Hz)						Output rate(Hz)		
AB	AC	BC	AD	BD	CD	AD	BD	CD
30(N)	30(N)	30(N)	30(Y)	30(Y)	30(Y)	-10±9	8±9	110±22
Input rate(Hz)						**Output rate(Hz)**		
AB	AC	BC	AD	BD	CD	AD	BD	CD
30(N)	0(N)	0(N)	0(Y)	0(Y)	30(Y)	1±8	20±9	49±20
Input rate(Hz)						**Output rate(Hz)**		
AB	AC	BC	AD	BD	CD	AD	BD	CD
30(N)	0(N)	0(N)	0(N)	0(N)	30(Y)	0	0	79±16

Table 3.3-Different input rate that affects the output rate fit by CIFIT

Results from CIFIT show agreement between the rates of ion exchange regardless of the initial condition. To test the accuracy and consistently of the experiment results, both from selective inversion experiments and CIFIT data fits, a series of different initial condition for the shaped pulse experiments were applied. Those initial conditions include: Sp1, sp1 and O1 (Figure 3.9). p11 is the power level of the selective inversion pulse, which corresponding to the power applied for inverted the resonance you want to invert. p11 is the power length of the selective inversion pulse. In shape pulse selective inversion experiments, this Gaussian pulse should have small bandwidth (less than hundred ppm), which means the p11 should be

long (hundreds micro seconds). O1 is the shift reference, and in shape pulsed selective inversion experiments, o1 should be set directly on the resonance you engaged to invert.

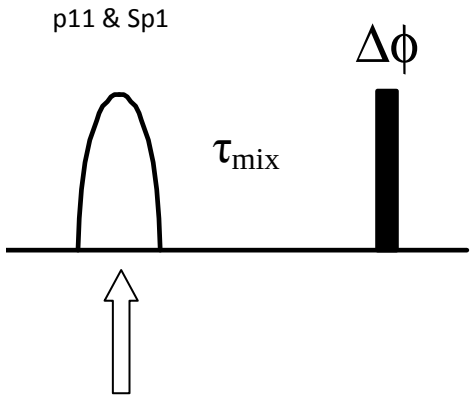

Figure 3.9-Pulse sequence for shaped pulse selective inversion experiment

The great challenging for using selective inversion experiments studying this material is the small peak separation in the spectrum, which makes it very difficult to optimize the selective inversion pulse, since a good selective inversion pulse should guaranty an fully inversion for the chosen resonance, and make sure the other resonance has been little affected. In general, in order to get a much smaller

selective inversion bandwidth, a very long p11 is needed, however this cannot work out in $Li_2MnP_2O_7$, because the T_1 relaxation time is too short for this material and the p11 should less than T_1. Despite the fact that we cannot reach the perfect condition when studying this material, we still have tried our best to make the selective inversion pulse as good as possible. However, it needed to be confirmed that different initial conditions should have no effects to the final exchange rates obtained from selective inversion experiments. Theoretically, changing the pulse length should not affect the exchange rate obtained from the experiments. In order to test that, different pulse lengths have been applied in the shape pulsed experiments, and under each pulse length, the power lever has been calibrate to obtain the maximum inversion of the inverted resonance. Table 3.4 clearly shows that when changing the pulse length, the exchange rate appears almost unchanged. This demonstrates that the data analysis is robust, and the experiment is not impacted by of the initial condition.

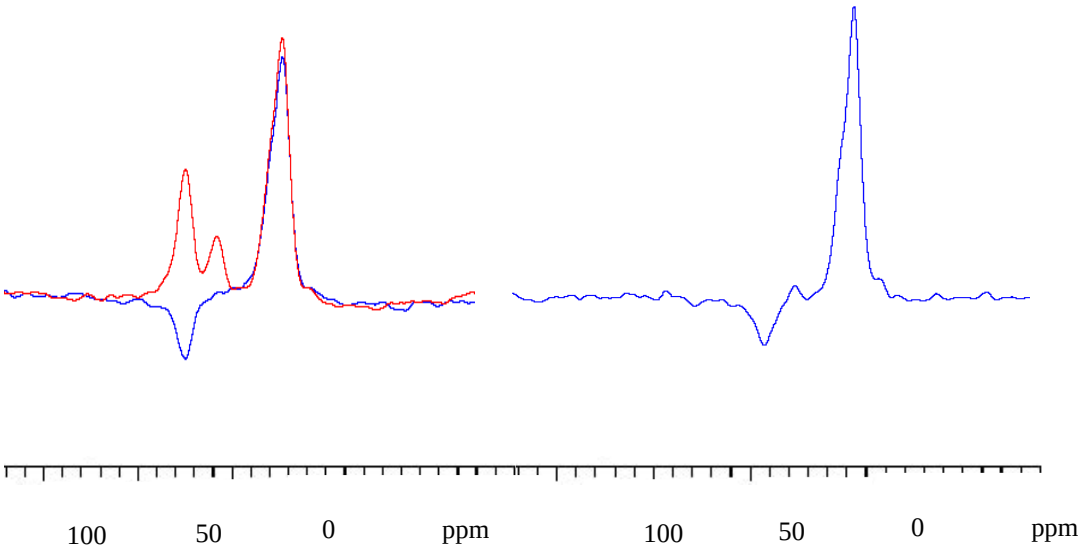

Conditions and percentage of inversion			Exchange Rates(Hz)
P11 = 750	sp1 = 28dB	72%	52±18
P11 = 1000	sp1 = 28dB	65%	47±19
P11 = 1500	sp1 = 30dB	55%	48±19

Table 3.4 -Different initial conditions and the exchange rates fit by CIFIT

Figures 3.10 clearly indicates that ^{6}Li selective inversion experiment was able to separate rate information from inherent T_1 properties. ^{6}Li T_1 experiment-NSI experiments, recorded over the same temperature range and mixing time period, are plotted beside the ^{6}Li SI experiments(When inverting resonance D). SI experiments

could detect dynamics while NSI experiments did not. For the SI data, it clearly shows that the buildup curves are influence by changes in the ion dynamics, while the NSI data remains relatively unchanged. [17] This further confirms that thermally driven chemical exchange is taking place for the resonance D.

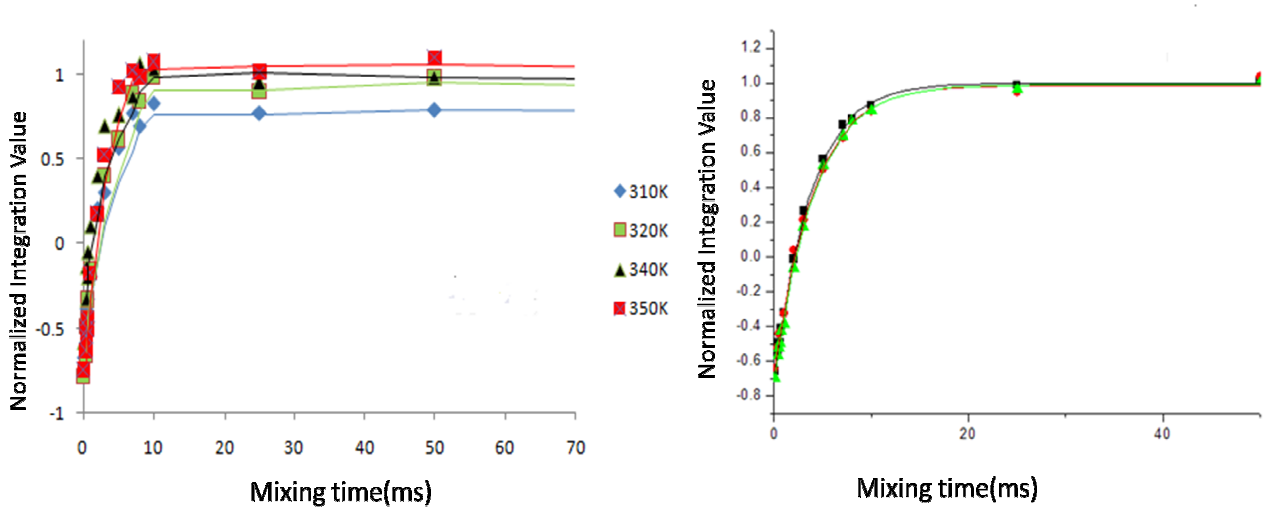

Figure 3.10- Plot integration to mixing time of resonance D for selective invertion data(left) and Non selective invertion data(right)

CD exchange pair was first studied using selective inversion experiments. Figure 3.11 plots the integration values of resonance D to the mixing time when invert C at several temperatures. The dataset was then fit by CIFIT and exchange rate was shown in Figure 3.11. Jump rates for C-D exchange pairs at different temperature were determined to allow the calculation of the activation energy, Ea. Figure 3.12 shows an arrhenius analysis of the natural log of the exchange rates over temperature plotted as

a function of inverse temperature. The energy barrier for CD exchange pair appears to be 2.1eV.

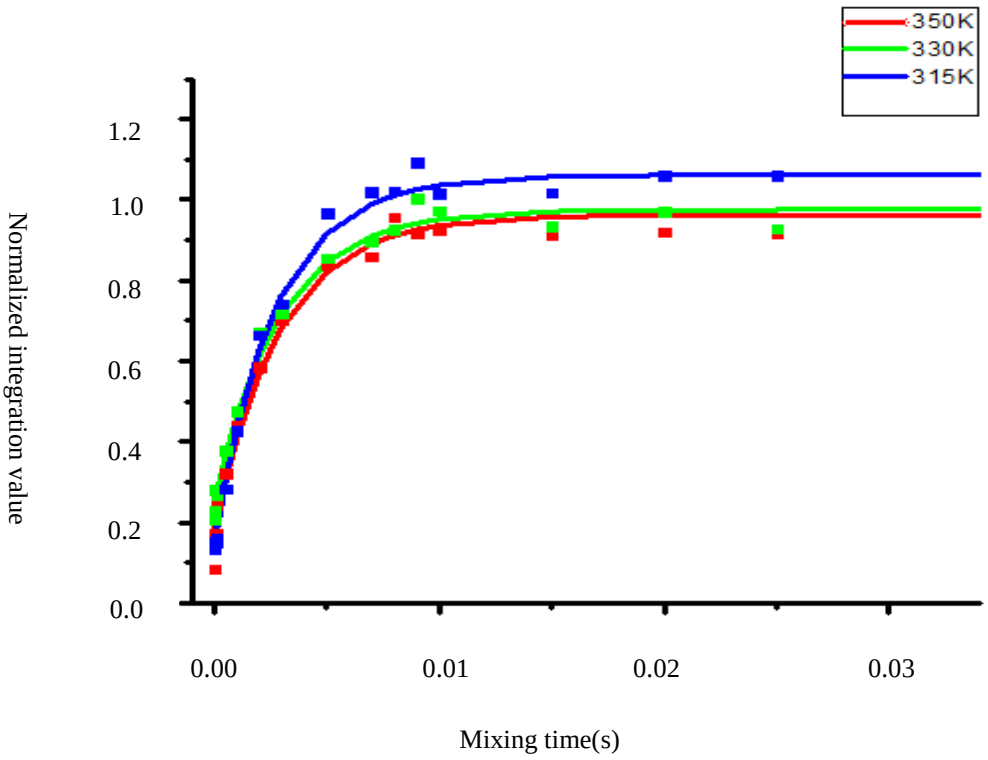

Figure 3.11- Plot integration to mixing time of resonance C when invert D at different temperature

In addition to resonance D, Resonance B was also inverted by SI experiments trying to extract the ion exchange rates, however, because the overal chemical shift differences between each resonance were quite small, it really became a great challenging to optimize selective inversion pulse. And as it shown in Figure 3.13, the

quality for those data sets were not high enough to obtain ion exchange rates by CIFIT.

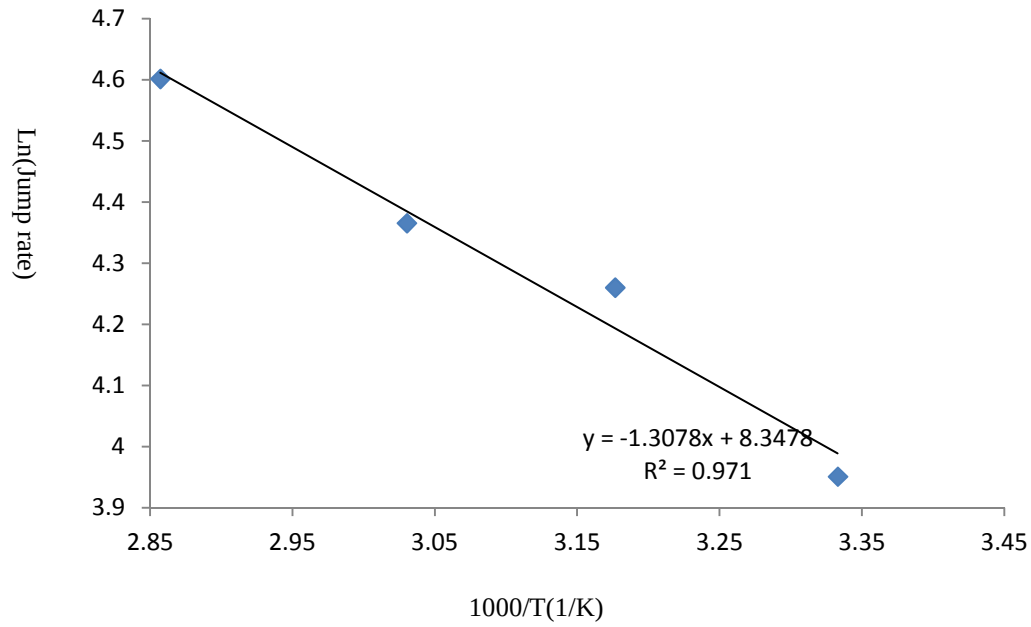

Exchange rate(Hz)			
300K	315K	330K	350K
54±18	70±17	79±16	100±20

Figure 3.12- Activation energy fit for CD exchange pair. Exchange rate at variable temperatures are shown below

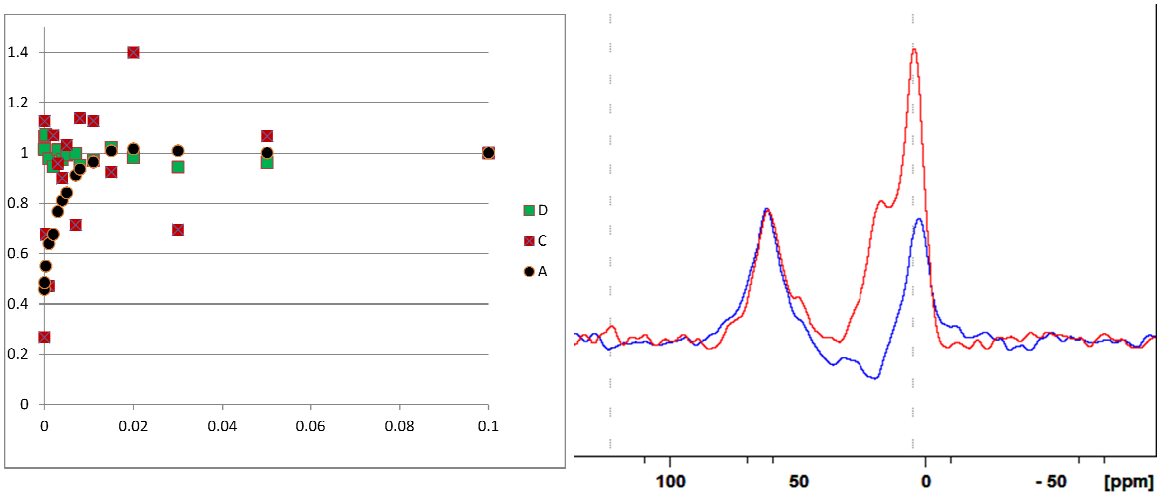

Figure 3.13- Plot integration to mixing time of resonance A when invert resonance B for selective invertion data(left) and comparasion of initial spectra and spectra after B is inverted (right)

3.3.5 Identification of Ion Exchange Pairs

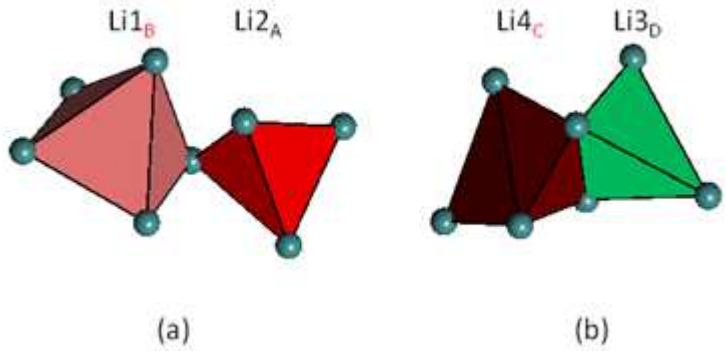

Figure 3.14- Two identified exchange pair from crystal structure data(left) and crystal structure of $Li_2MnP_2O_7$(right)

As it shown in Figure 3.14, two exchange pairs have been identified based on crystal structure and also our NMR experiments, which are ($Li1_B$, $Li2_A$) and ($Li3_D$, $Li4_C$). And table 3.5 below lists the geometry and structure information for these exchange pairs.

Exchange pair	Geometry of Li Ion Polyhedra	Li-Li Internuclear Distance(Å)	Bottleneck Area(Å^2)
$Li1_B$ -$Li2_A$	Corner(In tunnel)	3.073	3.52
$Li4_C$-$Li3_D$	Edge(In tunnel)	2.972	3.36
$Li1_B$-$Li3_D$	Cross tunnel	5.571	
$Li1_B$ - $Li4_C$	Cross tunnel	5.979	
$Li2_A$-$Li3_D$	Cross tunnel	5.217	
$Li2_A$ - $Li4_C$	Cross tunnel	5.990	

Table 3.5- Summary of all possible exchange pairs in $Li_2MnP_2O_7$

Figure 3.15 clearly shows that these two exchange pairs set in different tunnels, and it is clearly seen in this figure that only $Li1_B$ -$Li2_A$(red and pink), $Li4_C$-$Li3_D$(brown and green) should be able to exchange, since both pairs set in the same tunnel. While the other pairs of Li ions should not be able to exchange, because they are setting quite far away (Table 3.5), and they are obstructed by

phosphate group.

These two exchange pairs, however, have quite different exchange rate. We conclude that $Li4_C$-$Li3_{D,}$ according to the selective inversion experiments result, should have a slow exchange rate, while the $Li1_B$ -$Li2_{A,}$ according to the coalescence shown in variable temperature study, should have much faster ion exchange rate. When compared the exchange rate to other cathode materials, as it shown in Table 3.6, relatively fast ion exchange rates are shown for cathofe material like Li_2VOPO_4 and $Li_3Fe_2(PO_4)_{3.}$ At about 330K, Li_2VOPO_4 has exchange rate around 1000Hz, for $Li_3Fe_2(PO_4)_{3,}$ the ion exchange rate for exchange pair AB is over 600Hz at 310K, there is no experimental data for that exchange rate at 350K, but we can predict it should around 1000Hz as well based on arrehinius fit. On the contrary, for materials like Li_2VPO_4F(cathode material, still work electrochemically), which has a relatively slow ion exchange, the exchange rate is less than 100Hz just very similar to what we measured for CD exchange pair in $Li_2MnP_2O_7$. One thing to mention here, even Li_2VPO_4F has shown a relatively slow ion dynamic in NMR study, the electrochemistry still works fine for Li_2VPO_4F as a potential cathode material[18]. On the other hand, for AB exchange pair in $Li_2MnP_2O_7$, the jump frequency has been measured by variable temperature study, and is approximately 900Hz at 300K.

One thing to notice here is that even with this possible fast ion exchange between

$Li1_B$ -$Li2_{A,}$ poor electrochemical performance still observed for this material, and the reason still need to be studied in the future.

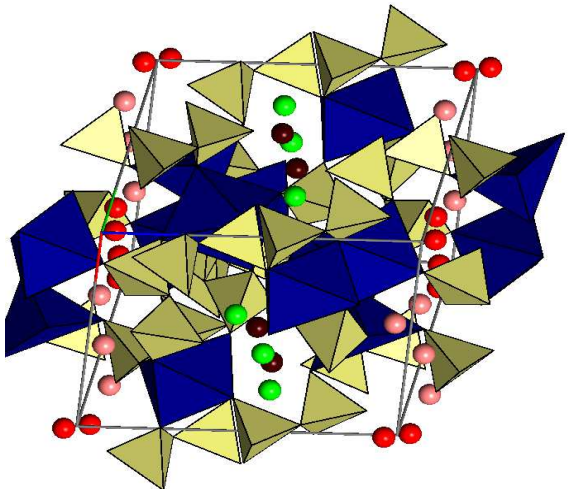

Figure 3.15- Crystal structure for $Li_2MnP_2O_7$, with red for Li1, pink for Li2, purple for Li3 and green for Li4. Mn is in blue and P is in yellow.

Cathode materials	Exchange pair	Temperature(K)	Exchange rate(Hz)
Li_2VPO_4F	AB	330-350	24-55
Li_2VOPO_4	BC	311-327	320-1100
$Li_3Fe_2(PO_4)_3$	AB	283-311	122-640
$Li_2MnP_2O_7$	CD	315-350	70-100
$Li_7La_3Zr_2O_{12}$	Electrolyte	298-323	4.7×10^{-4}-1.2×10^{-3}(S/cm)

Table 3.6- Summary of exchange rates for some exchange pairs in different cathode materials

The energy barriers and jump rates measured in $Li_2MnP_2O_7$ were evaluated in relation to structural constraints presents in the host framework. In the previous report of the ion dynamics in other materials, the energy barriers of the ion hopping were found to be higher in ion pairs where longer internuclear distances coupled with smaller bottlenecks of diffusion. The highest energy barrier observed has the most open bottleneck area and the shortest internuclear distance.

3.4 Summary

In this chapter, a combination of variable temperature experiments and 1D shape pulsed selective inversion methods were used to identify and quantify the structural and dynamic features of $Li_2MnP_2O_7$. Slow dynamic was confirmed by variable temperature study and ion exchange timescales is obtained by 1D selective inversion measurements. CIFIT was used for data analysis. Lastly, ion exchange pairs were identified for $Li_2MnP_2O_7$. The energy barrier for CD exchange rate turns out to be 2.1eV, relatively fast ion exchange is confirmed by variable temperature study of $Li_2MnP_2O_7$. The dynamic studied shown in this chapter help us understand not only the Li ion mobility in $Li_2MnP_2O_7$ but also in other lithium pyrophosphate materials

such as $Li_2FeP_2O_7$, $Li_2VP_2O_7$ and $Li_2(Fe_{1-y}Mn_y)P_2O_7$. These series of pyrophosphate materials show a small change in lattice parameters, but form a complete identical structure with a monoclinic 3D framework and $P2_1/c$ symmetry. Therefore, those compounds should have the similar Li ion pathway as we already identified in $Li_2MnP_2O_7$ system.

The electrochemistry of $Li_2MnP_2O_7$ is not very satisfactory by now[3]. The inactivity of Mn-species is no surprise as very low activity of Mn is common for many other polyanionic systems, presumably because of lower electronic conductivity of Mn compounds, Jahn−Teller distortion caused by Mn^{3+} ion. And this poor ion conductivity might be well improved by special technique like nanosizing and carbon coating. Although the electrochemical capacity of $Li_2MnP_2O_7$ is disappointing at the moment, high redox potential is observed for this material. The cyclic voltammetry for $Li_2MnP_2O_7$ with an extended voltage range of 1.5-5.5 V clearly shows two oxidation peaks at 4.5V and 5.3V[3], which should corresponding to Mn^{2+}/Mn^{3+} and Mn^{3+}/Mn^{4+} redox couples. What's more, in the $Li_{2-x}(Fe_{1-y}Mn_y)P_2O_7$ systems, even though the inclusion of Mn does not improve the electrochemical capacity of $Li_{2-x}(Fe_{1-y}Mn_y)P_2O_7$ pyrophosphates, it is able to push the Fe^{3+}/Fe^{2+} redox potential close to 4 V in a phosphate-based cathode system[19].

3.5 References

(1) Adam, L., A. Guesdon, and B. Raveau, Journal of Solid State Chemistry, 2008. 181(11): p. 3110-3115.

(2) Zhou, H., et al., Chemistry of Materials, 2010. 23(2): p. 293-300.

(3)Bain,A. D.; Fletcher, D.A.Mol. Phys. 1998, 95, 1091

(4) Morgan, D., A. Van der Ven, and G. Ceder, Electrochemical and Solid State Letters, 2004. 7(2): p. A30-A32.

(5) Zaghib, K., et al., Journal of Power Sources, 2006. 160(2): p. 1381-1386.

(6) Nagaura, T.; Tozawa, K. Prog. Batteries Solar Cells 1990: p.209

(7)Davis, L.J.M., I. Heinmaa, and G.R. Goward, Chemistry of Materials, 2010. 22(3): p.769-775.

(8) Grey, C.P. and N. Dupre, Chemical Reviews, 2004. 104(10): p. 4493-4512.

(9)Kim, J., et al., Journal of the American Chemical Society. 132(47): p. 16825-16840.

(10) Adam, L., A. Guesdon, and B. Raveau, Journal of Solid State Chemistry, 2008. 181(11): p. 3110-3115.

(11) Zhou, H., et al., Chemistry of Materials, 2010. 23(2): p. 293-300.

(12) Stout, G.H. and L.H. Jensen, X-ray Structure Determination: A Practical Guide.

(13) Dominko, R., et al., Electrochemistry Communications, 2006. 8(2): p. 217-222.

(14) Yabuuchi, N., et al., Dalton Transactions, 2010. 40(9): p. 1846-1848.

(15) Yabuuchi, N., et al., Electrochemistry. 78(5): p. 363-366.

(16) Davis, L.J.M., I. Heinmaa, and G.R. Goward, Chemistry of Materials, 2010. 22(3): p.769-775.

(17) Grey, C.P. and N. Dupre, Chemical Reviews, 2004. 104(10): p. 4493-4512.

(18) Ellies, et al., Chemistry of Materials, 2011. 23: p. 5138-5148

(19) Furuta, et al., Chemistry of Materials, 2012. 24: p. 1055-1061

Chapter 4: Structure Information and Quantification of Li Ion Mobility of $Li_2FeP_2O_7$

4.1 Introduction

Structural and electrochemical details of $Li_2FeP_2O_7$ were first published in by Zhou.et.al[1]. Fe atoms occupy three crystallographic sites, Fe1, Fe2 and Fe3. Iron Fe1 is coordinated as FeO_6 octahedra, and Fe2 and Fe3 are coordinated as distorted FeO_5 pyramids. Li atoms are coordinated as LiO_4 tetrahedra or LiO_5 trigonal bipyramids, forming a quasi-two-dimensional network along the b-c plane in the $P_{21/c}$ setting, which provides a possible path for Li diffusion[2].

For $Li_2FeP_2O_{7,}$ its reversible electrode operation at 3.5V vs Li was identified. The gravimetric theoretical capacity is 117mAg/h for $Li_2FeP_{22}O_{7\,,}$ which corresponding to one lithium extracted during electrochemical process[1], This is because the Fe^{3+}/Fe^{4+} redox potential falls outside of the voltage range created by most lithium battery electrolytes used(5V, $LiPF_6$) , which leads to the result that only the first lithium ion can be cycled in current commercial electrolyte. However, cyclic voltammetry studies reveals second oxidation peaks, at 5.1 V for $Li_2FeP_2O_7$[1], suggesting that Fe^{3+}/Fe^{4+} redox couples are active, which indicated that the second lithium ion can be cycled if a stable high-voltage electrolyte is found and electronic conductivity of the

pyrophosphate is enhanced.

We know that cathode materials involve either a distinct two-phase or a single-phase throughout the process. Consider a two-phase process, where the free energy G as a function of x(number of remaining Li ion in cathode) has two branches, the system will break into two different phases between x_1 and x_2. Therefore, at those states when x between x1 and x2, the system consists of domains of the two phases, domains,. Increasing x causes the domains of the phase with larger composition(x_2) to grow at the expense of the phase of lower composition(x_1). Such a transition between two phases is called a first-order transition.[3] Since the compositions of the coexisting phases do not change, the chemical potential is constant in this two-phase region. Which means in an electrochemical curve of the cell when we plot voltage to x, a plateau should be observed in a two-phase region. (Figure 4.1)

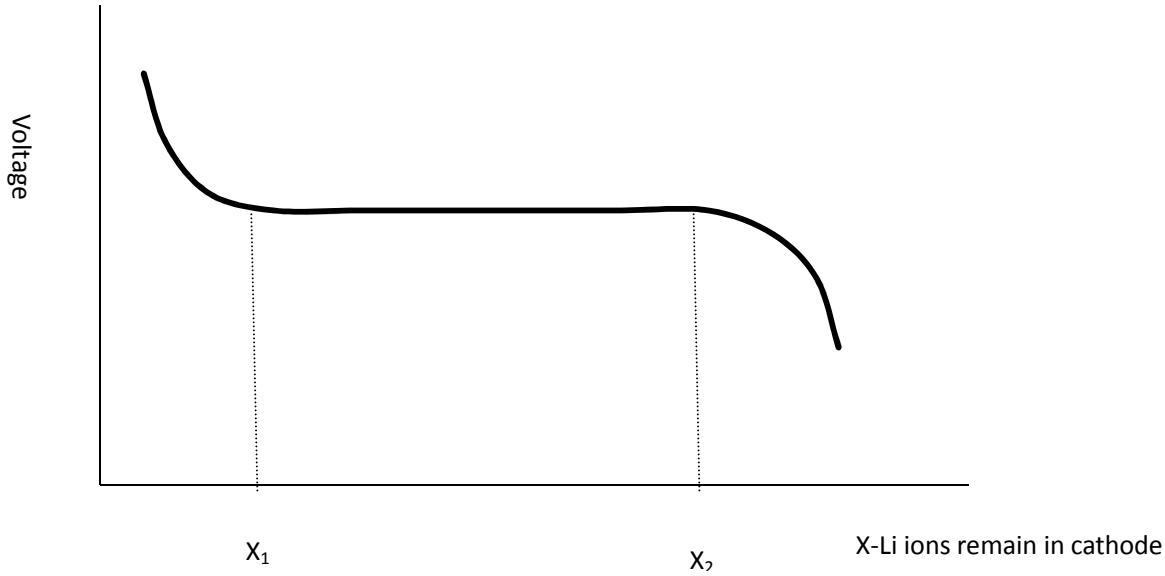

Figure 4.1-Electrochmical curve of voltage to x shown two-phase reaction

On the other hand, solid-solution process belongs to continuous phase transitions, which also called as higher-order transitions, In which there is no phase separation existence[3]. Therefore, when we plot the voltage to x in an electrochemical curve, there is no plateau can be observed, and the voltage should be continuously change with x as it shown in figure 4.2.

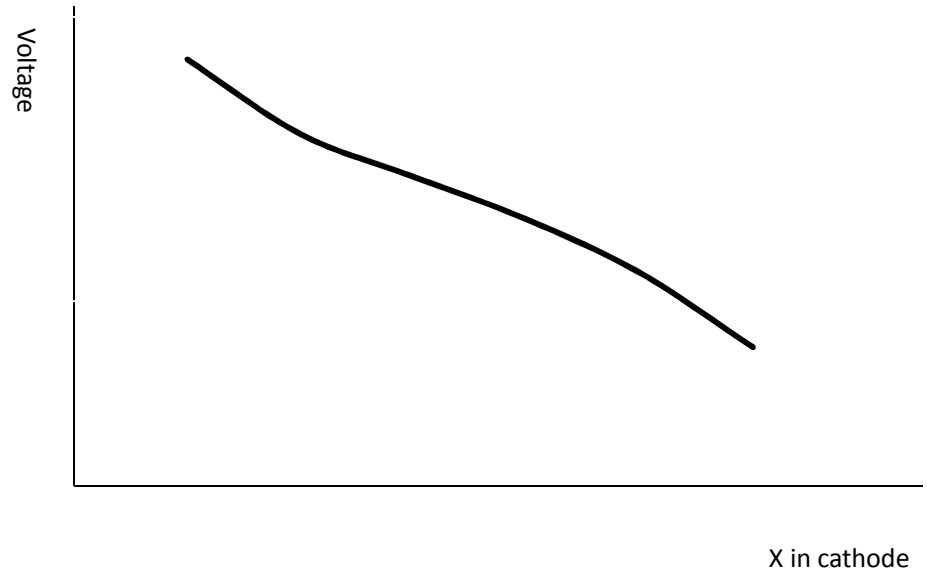

Figure 4.2-Electrochmical curve of voltage to x shown solid-solution process

The crystal structure and electrochemical performance of $Li_2FeP_2O_7$ has been already reported and confirmed. However, the underlying electrochemical reactions mechanism is not clearly known. A detailed understanding of an active reaction mechanism is important for further development of cathode performance. Kim et al. did some preliminary work for this material using neutron diffraction(ND) and X-ray diffraction(XRD). The crystal system and space group were determined to be monoclinc $P2_1/c$, which is identical to previous study. However, the neutron diffraction(ND) identified a different lithium positions and partial occupancies in five different Li sites for $Li_2FeP_2O_7$ compare to previous work by Zhou.et.al. What's more,

further ex-situ XRD showed that the charging/discharging of $Li_2FeP_2O_7$ occurred primarily via a two-phase reaction with a slight solid solution behavior[4].

Their XRD pattern data were collected over a 2θ range of 10 - 60˚ with a step size of 0.02˚ using the X-ray diffractometer (Rigaku,D/MAX 2500) equipped with Cu Kα radiation. And then refined by the Rietveld method using Fullprof software.

They investigated the structural evolution of $Li_{2-x}FeP_2O_7$ electrodes in a Li cell using ex situ XRD analysis. They cycled their batteries with $Li_{2-x}FeP_2O_7$ as electrode at a low current rate, and then using XRD measurements to study cycled material in different charge or discharge states. The series of XRD patterns corresponding to both charge and discharge process are shown in Figure 4.3(a) and (b), respectively. As it is shown in the amplified figure in the inset of Figure 4.3(a), a new set of peaks appeared at 12-14˚ during charging process, and these peaks will disappear during discharge process as it shown in Figure 4.3(b). These series of new peaks are also observed in the XRD patterns of their independently synthesized $LiFeP_2O_7$ sample, which are shown in Figure 4.3(a) and (b) as well. They conclude this new peaks denoted as (*) correspond to the (110) and (011) peaks of $LiFeP_2O_7$. This observation indicates that the delithiation of $Li_{2-x}FeP_2O_7$ occurred via a two-phase reaction between $Li_{2-x}FeP_2O_7$ and $LiFeP_2O_7$. And the initial stages of charge slight peak shifts were attribute to some degree of solid solution behavior.

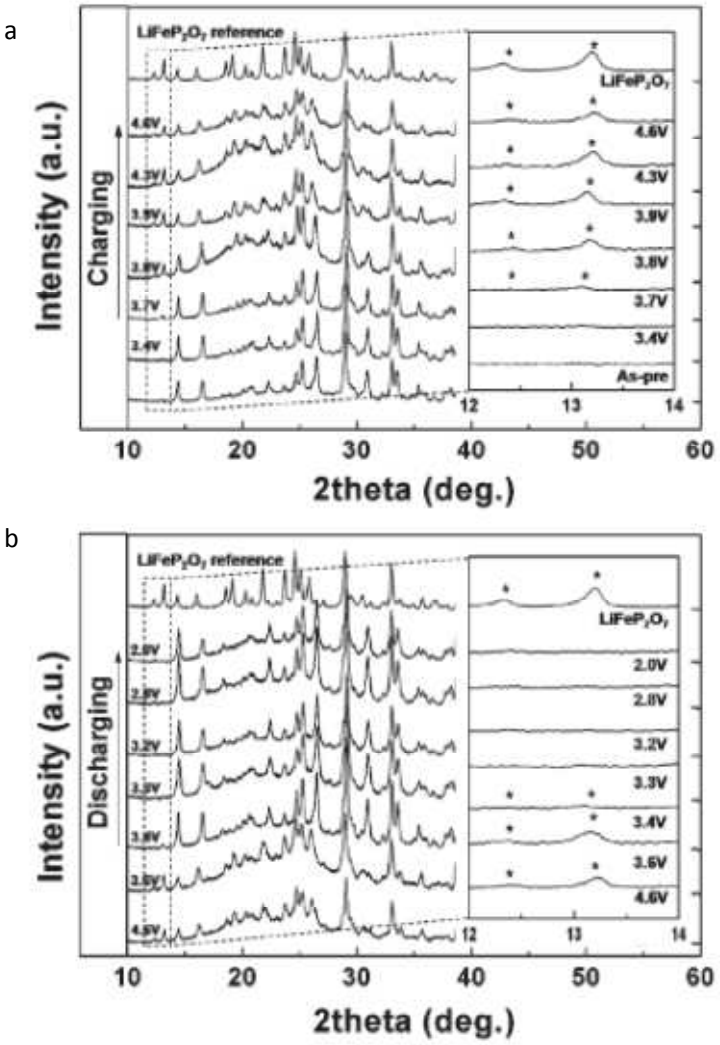

Figure 4.3- XRD patterns of cycled $Li_{2-x}FeP_2O_7$ in charge(a) and discharge(b) by Kim et.al.

Shimizu et al. published the structural analysis of the electrochemical redox mechanism of $Li_2FeP_2O_7$ cathode, and shown quite different conclusion about the

electrochemical process.

Their X-ray powder diffraction patterns were obtained using a Bruker-AXS D8 Advance diffractometer equipped with Co Kα radiation(0.77889) operating at 35 kV and 40 mA. Typically, the scans were measured with the Bragg–Brentano geometry in the 2θ range of 15–80° with the step interval of 0.028–0.035°. Same as the literature mentioned previously, ex site XRD analysis in quasi-equilibrium states were used to probe the structural change during one-electron reaction in $Li_{2-x}FeP_2O_7$(x=0-1). Their XRD pattern for first and second cycles are shown in Figure 4.4, It's clearly shown in this series of patterns that peak positions had a continuous change, during charging/ discharging, all the peaks upshift/downshift slightly, peak intensity ratios changed drastically, and all the bragg reflections were fully indexed with the $P2_1/c$ monoclinic lattice, which means those XRD patterns didn't indicate clear evidence of the phase separation, and suggest the electrochemical reaction should be a solid-solution (de)lithiation mechanism. As it shown in Figure 4.5 , when zoom in at the small angels, they observed a similar change of relative intensity for the Bragg reflections as Kim et.al, and . some strongly enhanced peaks are very weak in the initial state. Contrary to former literature, since those peaks are indexed and allowed reflections for the $P2_1/c$ monoclinic lattice, they owned these new, actually enhanced, peaks to the structure rearrangement(e.g., atomic site change).

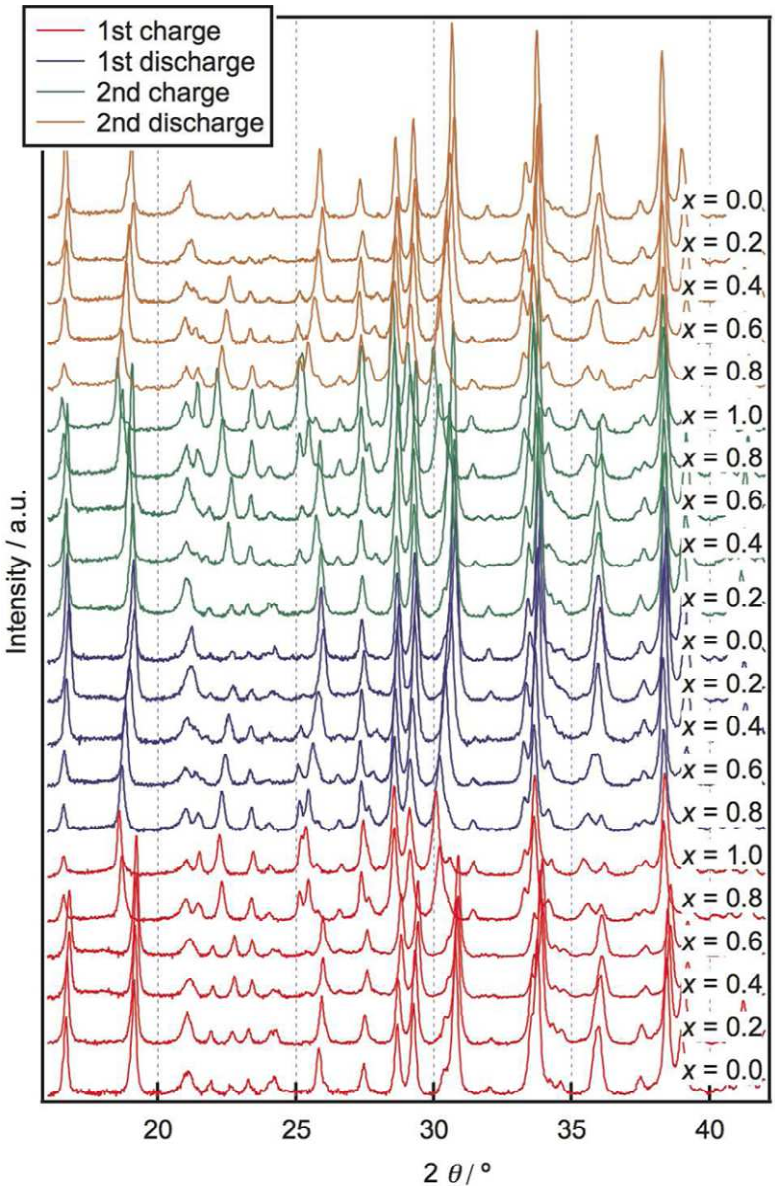

Figure 4.4- XRD patterns of cycled $Li_{2-x}FeP_2O_7$ by Shimizu et al.

They also study the open circuit voltage curve to confirm this solid-solution mechanism. The OCV curve(Figure 4.6) did not show any flat voltage regions,

indicating the reaction proceeds without the separation of two phases.

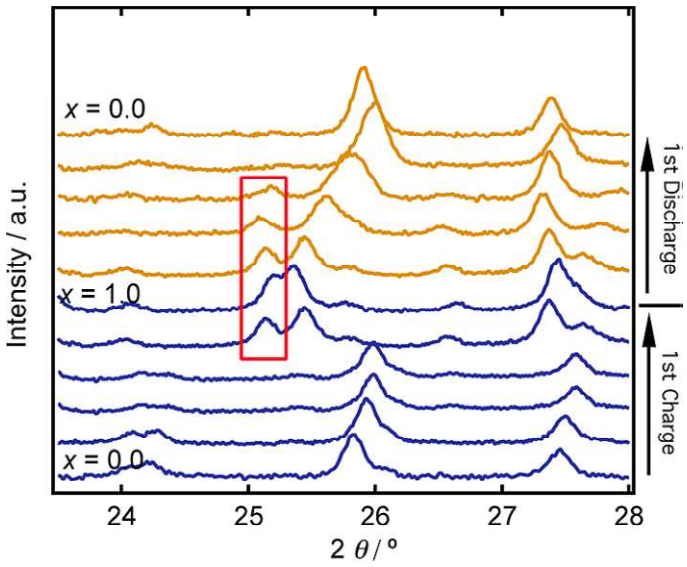

Figure 4.5- Zoom in XRD patterns of cycled $Li_{2-x}FeP_2O_7$ by Shimizu et al

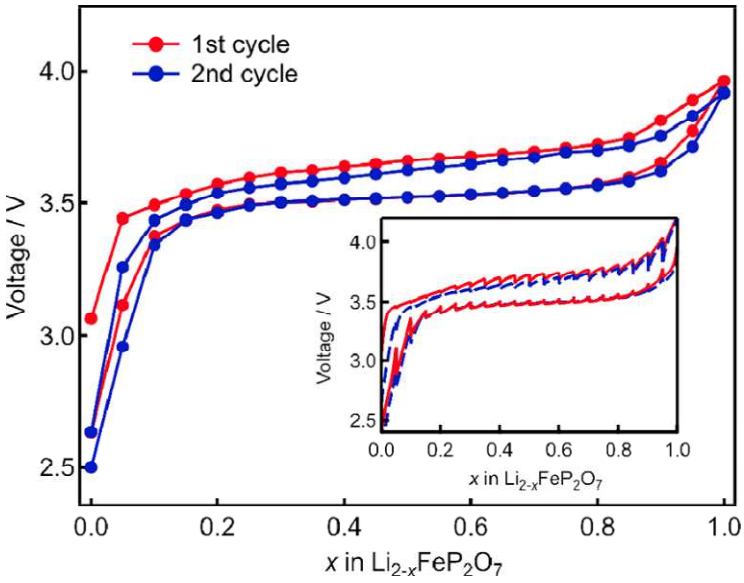

Figure 4.6- Open circuit voltage curves for $Li_2FeP_2O_7$

Figure 4.7 shows the comparision of $LiFeP_2O_7$ and $Li_2FeP_2O_7$ spectrum, X-ray diffraction patterns of the pristine $Li_2FeP_2O_7$ and oxidized material, $LiFeP_2O_7$. Lattice parameters in $P2_1/c$ setting are a = 11.01847(4) Å, b = 9.75536(3) Å, c = 9.80517(3) Å, β = 101.5416(2)° for $Li_2FeP_2O_7$, and a = 11.39786(17) Å, b = 9.6042(15) Å, c = 9.84162(11) Å, β = 102.2967(8)° for $LiFeP_2O_7$. Since we observed continues very small change in ex-XRD studies of the cycled $LixFeP_2O_7$, we believe a solid-solution process should be reasonable.

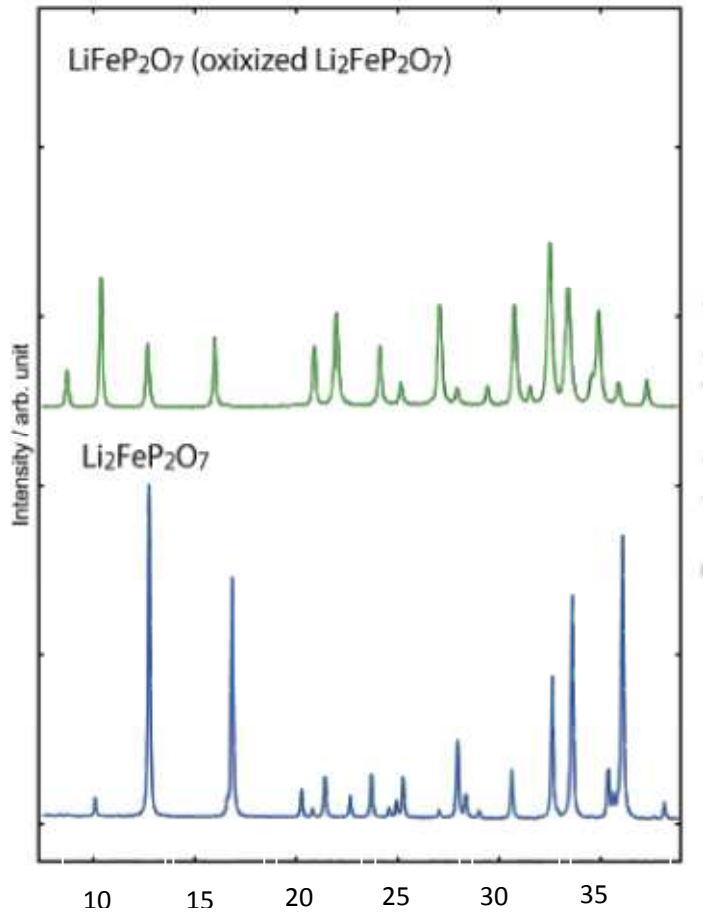

Material	$Li_2FeP_2O_7$	$LiFeP_2O_7$
Space group	$P2_1/c$	$P2_1/c$
Lattice constant		
a/Å	11.01847(4)	11.39786(17)
b/Å	9.75536(3)	9.6042(15)
c/Å	9.80517(3)	9.84162(11)
β	101.5416(2)	102.2967(8)

Figure 4.7-Comparision of XRD pattern and unit cell parameters for $LiFeP_2O_7$ and $Li_2FeP_2O_7$

4.2 Experimental

4.2.1 Sample Preparation

$Li_2FeP_2O_7$ sample studied here were prepared in our group and also by collaborators at the New York State University. Samples prepared in our group were synthesized via a solid-state reaction first described by Nishimura *et al.*[2]. Briefly, 0.01 mol lithium carbonate(Li_2CO_3) , 0.01 mol iron oxalate dihydrate ($FeC_2O_4.2H_2O$),

and 0.02mol diammonium hydrogen phosphate ($(NH_4)_2HPO_4$) were mixed in acetone, and then ground for 30 min. The obtained slurry was evaporated under vacuum at 300°C for 6 hours (2 hours from room temperature to 300°C) and reground. The precursor was then heated again at 600°C for 12 hours in an argon flow.

The sample prepared by our collaborators were synthesized via “wet” method published by Zhou *et al.* [1], Briefly, 0.01 mol lithium acetate($Li(CH_3COO)$) , 0.01 mol iron acetate ($Fe(CH_3COO)_2$), and 0.02mol ammonium phosphate ($NH_4H_2PO_4$) were dissolved in 100 mL of distilled water. The self-adjusted pH values of all of the solutions were determined to be 4.5-5. The solutions were stirred and evaporated on a hot plate in the hood, followed by vacuum oven overnight drying at 90°C. Finally, the solids were annealed in a H_2/He atmosphere at temperatures ranging from 400°C to 700°C with intermediate grinding.

4.2.2 Powder XRD

X-ray diffraction(XRD) patterns of the synthesized sample was obtained using a PANalytical diffractometer from 2θ= 10-45˚ with Cu Kα radiation at 45kV and 35mA.

Figure 4.8 shows the refinement of X-ray diffraction(XRD) patterns of synthesized $Li_2FeP_2O_7$ using GSAS. No obvious impurity is seen in the figure, and it should be very close to a single phase sample.

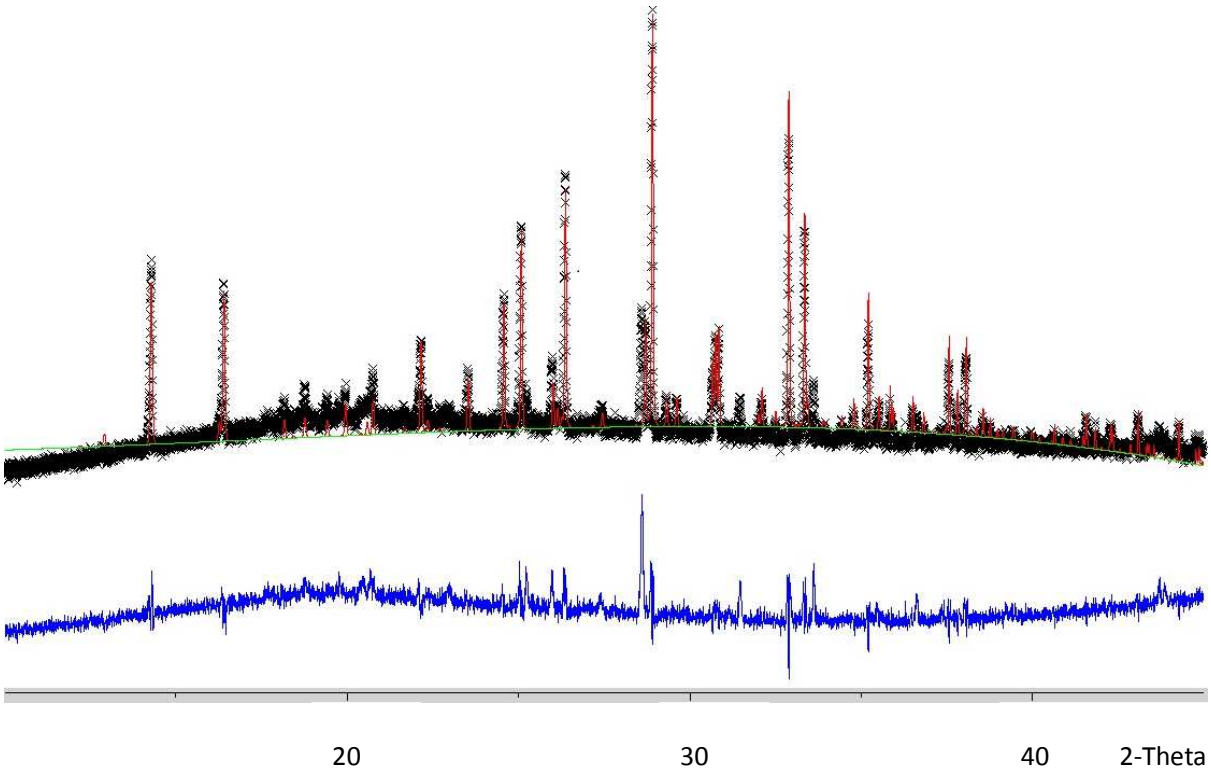

Figure 4.8-refined X ray diffraction(XRD) pattern of synthesized $Li_2FeP_2O_7$, red line is the calculated result, while the black line shows the experiment data. Blue line indicates the difference map.

NMR measurements for these two $Li_2FeP_2O_7$ samples were performed on a Bruker AV-300 spectrometer using a custom made 1.8 mm probe at Larmor frequencies of 116.6 MHz for ^{7}Li , and 44.2 MHz for ^{6}Li. All $^{6,7}Li$ shifts were

reference to 1M ^{6,7}LiCl (0 ppm). Measurements carried out here includes room temperature 1D ^{7}Li MAS measurements of each sample. ^{7}Li 1D spectra were obtained using a Hahn-echo pulse sequence(90° – τ - 180°) with 90° pulses at 3.5 µs and recycle delays of 0.2s. Spin lattice relaxation times(T_1) were obtained using standard inversion recovery sequence included in the Bruker software package.

4.2.3 Electrochemical Measurements

Electrochemical properties of $Li_2FeP_2O_7$ was examined with Li metal as the negative electrode. Positive electrodes consisted of 70 wt% $Li_2FeP_2O_7$, 20 wt% carbon black, and 10 wt% PVDF. PVDF was already dissolved in N-methyl pyrrolidone with 2 %wt. The electrolyte was 1M $LiPF_6$ dissolved in a mixture solution of ethylene carbonate(EC) and dimethyl carbonate(DMC) in a volume ratio of 1:1. The assembling of cells was done in glove-box filled with argon. The cycling was performed at room temperature between 1.8V and 4.5V.

The electrochemical properties of $Li_2FeP_2O_7$ were tested at room temperature, with Figure 4.2 showing the charge and discharge curves. Batteries were cycled

between 1.8V and 4.5V measured at a C/50 rate(C is the discharge rate, C/50 corresponds to discharging the cell over a period of 50 hours).

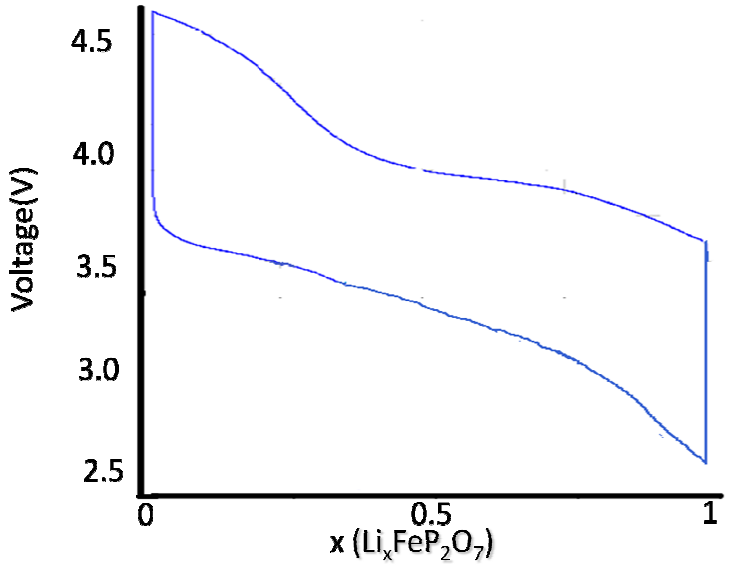

Figure 4.9-Charge and discharge curve for synthesized $Li_2FeP_2O_7$

Figure 4.9 indicates an electrochemical activity centered around 3.5V vs Li and that is higher than the plateau voltage of $LiFePO_4$, which is promising. For the batteries with no technical effort(such as carbon coating and nanosizing), about 0.8 Li can be extracted, which means the capacity can reach 90mAh/g(117mAh/g for the theoretical capacity).

4.3 Result and Discussion

4.3.1 ^{6,7}Li MAS NMR of $Li_2FeP_2O_7$

The 1D MAS = ^{7}Li spectrum for $Li_2FeP_2O_7$ for each samples are shown in figure 4.10, as it indicates here, the linewidths are very broad(about 200ppm for the isotropic) mainly because the paramagnetic Fe^{2+} center causes the short T_1 of electrons, which results in a short T_2* for these lithium site, leading to indistinguishable lithium sites. There should be 4 peaks corresponding to 4 unique crystallographic lithium site, but now those peaks are overlap with each other and show a single broad isotropic resonance, with series of spinning sidebands in the spectrum.

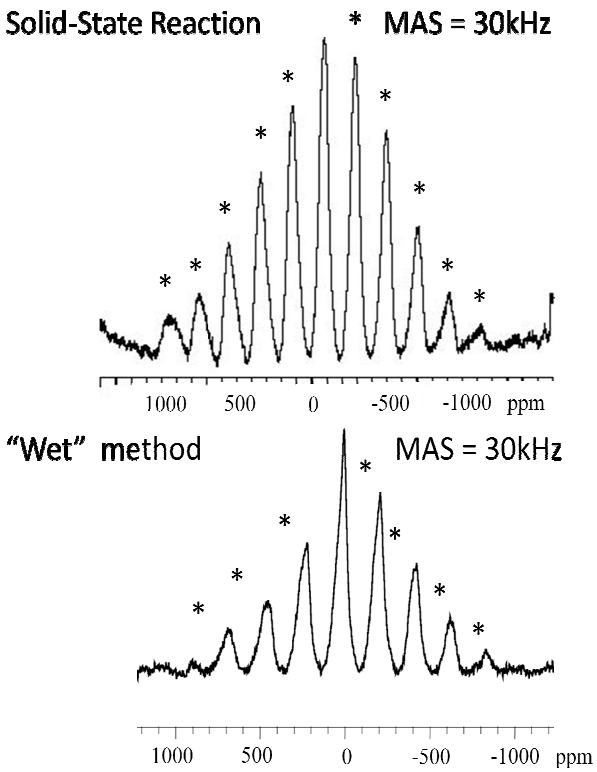

Figure 4.10-^{7}Li NMR spectrum of synthesized $Li_2FeP_2O_7$

Nevertheless, there is still some information that can be extracted from these low resolution spectra. It is shown clearly that these two samples obtained by different synthesis method have quite different lineshape in their spectrum, which indicates that, even though these two sample have the same space group and similar lattice parameter, they have different lithium occupancy.

Since it is interesting to find out if the differences in lithium occupancy will give us different lithium ion mobility, a preliminary deconvolution for both spectrum were done using DMFIT. The deconvolution results were shown below in Figure 4.11,

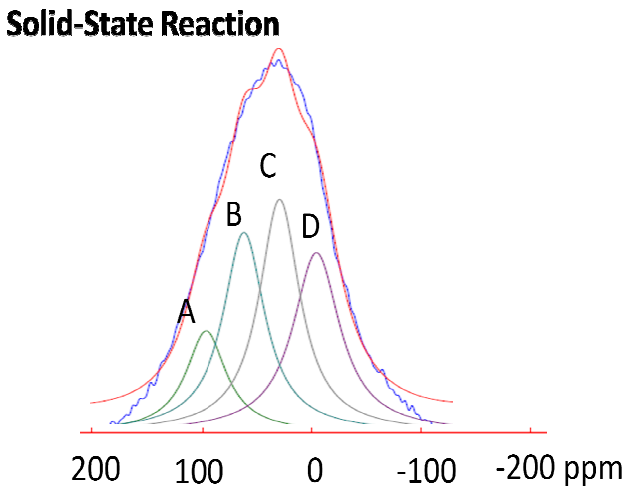

Shift(ppm)	Assignment	Integration ratio	Lithium occupancy
57ppm	Li A	0.5	0.48
36ppm	Li B	0.94	1
17ppm	Li C	1	1
-3ppm	Li D	1	1

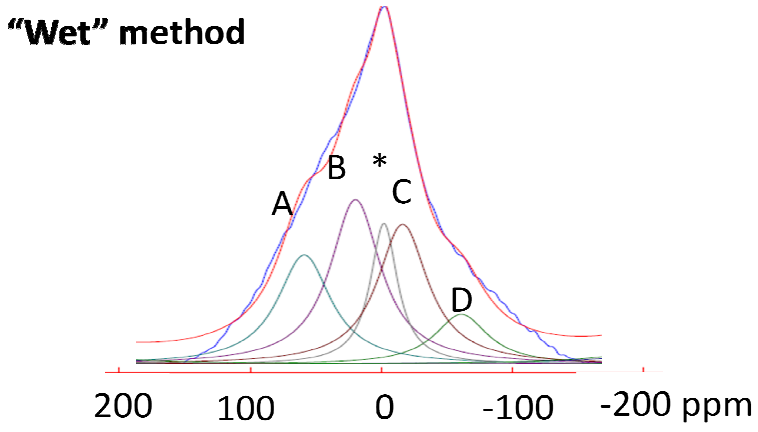

Shift(ppm)	Assignment	Integration ratio
54ppm	Li A	0.8
22ppm	Li B	1
-7ppm	Li C	0.96
-46ppm	Li D	0.4

4ppm	impurity	0.03

Figure 4.11- deconvolution spectrum of isotropic region and integration result for $Li_2FeP_2O_7$ synthesized by two methods

As is shown above, for sample prepared by "wet" method, integration over the entire sideband manifold gave A : B : C : D the ratio of 0.8 : 1 : 0.96 : 0.4, corresponding to the lithium occupancy for each site. The impurity peak takes about 3% in the whole spectrum

For sample prepared by solid-state reaction, Integration over the entire sideband manifold gave A : B : C : D the ratio of 0.5 : 0.94 : 1 : 1.

According to the crystal structure data obtained by Nishimaru.*et.al* using XRD, three of the lithium sites are fully occupied, and the occupancy for the rest one is 0.457[2], which matches NMR result well.

4.3.2 ^{7}Li MAS Study of Electrochemically Cycled $Li_xFeP_2O_7$

In this section, the electrochemical reaction mechanism concerning the one electron (de)lithiation process in $LixFeP_2O_7$ was examined(from x = 2 to x = 1),

combining with the structural and electrochemical analysis. The electrochemical reaction was stopped at several points both on charge and discharge curve when $Li_2FeP_2O_7$ was cycled to points found midway between voltage plateaus. Here ^7Li MAS NMR measurements are used to characterize Li environments in $Li_2FeP_2O_7$ after being electrochemically cycled to these particular points along the voltage plateaus. Figure 4.15 shows the experiments used to extract 1Li from $Li_2FeP_2O_7$. The stopping points are shown on the curve, The MAS spectra of the pristine and cycled samples are shown in Figure 4.12 . In this experiment, due to the low sample size of electrochemically cycled cathode materials, KBr has been used when packing the samples in the 1.8mm rotors, and is used to fill half of the rotor first, then the grounded cycled cathode material is packed into the rotors, to make sure the cathode material is located in the central part of the rotor. At last, more KBr is used to filled up the rotor. One thing to mention here regarding the cathode material is that the amount of cathode materials being packed into the rotors might have minor difference, which would cause a small for the signal obtained by NMR experiments. However, we are interested in the relative intensities of the resonances.

0

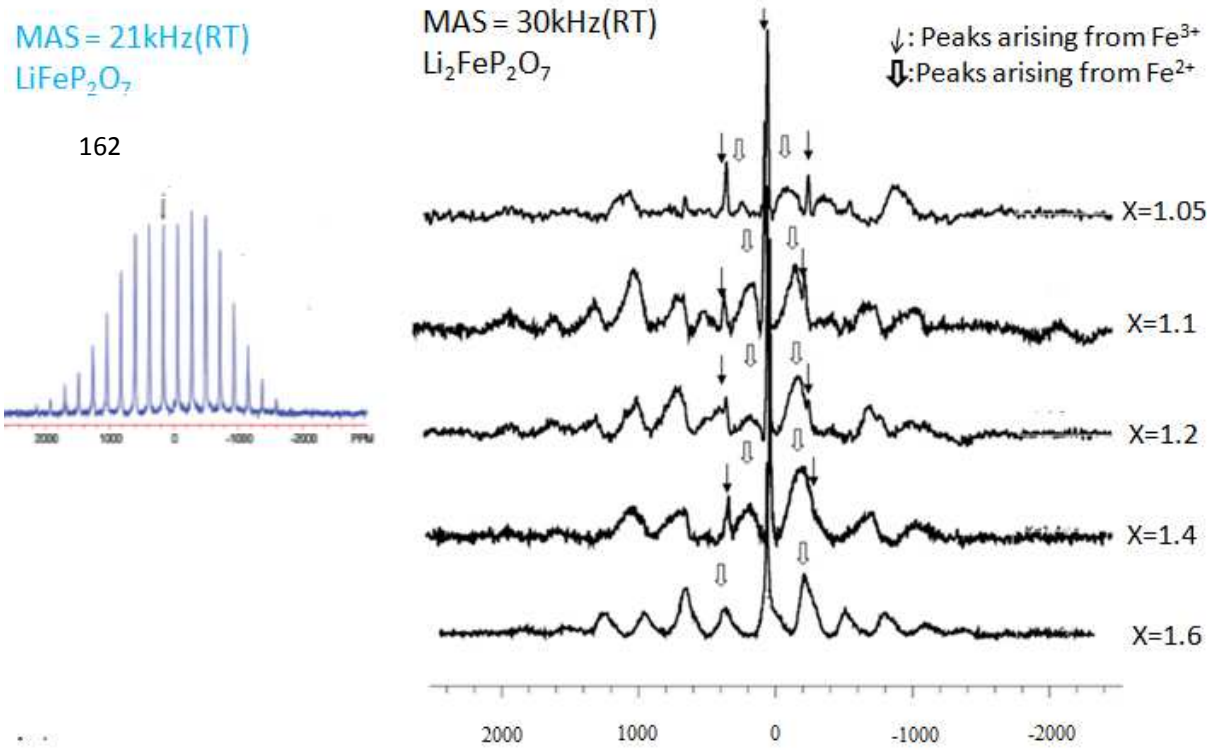

Material	**$Li_2FeP_2O_7$**	**$LiFeP_2O_7$**
Isotropic Chemical shift	0ppm	162ppm

Figure 4.12-^{7}Li NMR spectrum of the $LiFeP_2O_7$ (Left) ^{7}Li NMR spectrum as-prepared $Li_2FeP_2O_7$ and the cycled material(right) The white arrow corresponding to peaks arising from Fe^{2+}, black arrow corresponding to peaks arising from Fe^{3+}

Figure 4.12 shows a series of ^{7}Li MAS spectrum at spinning speed equal to 30kHz. There is an observed series of narrow peaks shown in the ^{7}Li MAS NMR spectrum after about 0.6Li was extract,which should be attribute to the Li sites arising from the effect of Fe^{3+}. The appearance of spinning sidebands for the narrow isotropic

resonance around 0ppm indicates that the signal should come from the paramagnetic Li sites rather than the diamagnetic electrolyte($LiPF_6$). While for the series of broad peaks shown on spectrum throughout the whole (de)lithiation process, we attribute those peaks to the Li sites arising form the effect of Fe^{2+}. We assigned the Li near Fe in oxidation 3+ to those narrow peak while the Li near Fe in oxidation 2+ to those broad peak, this is mainly based on determination of the linewidth:

$$FWHM = T_2^{-1} = T_{2N}^{-1} + (\frac{A_H}{\hbar})^2(\frac{T_{1e}}{8})$$

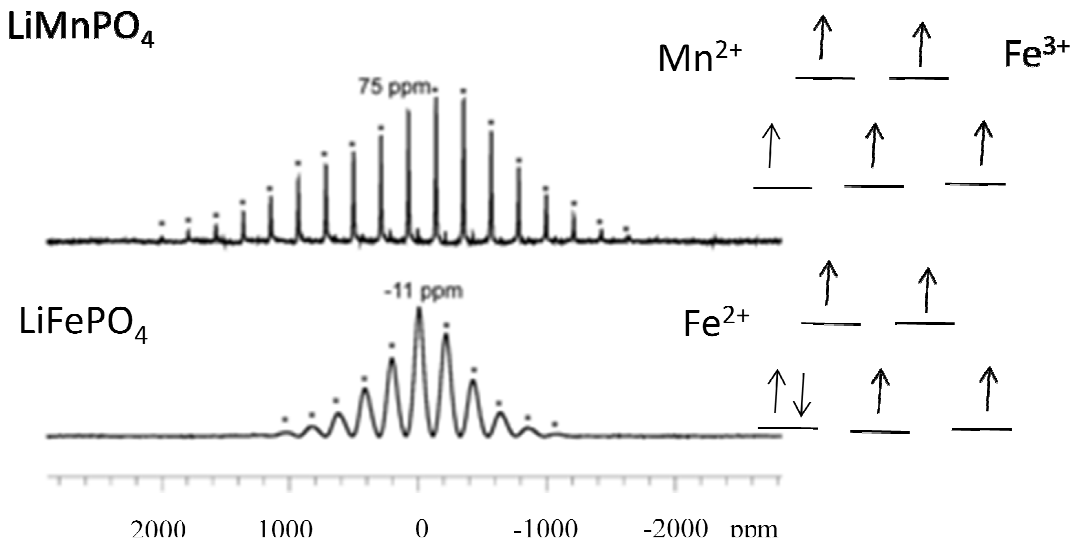

Figure 4.13- ^{7}Li MAS spectrum for $LiMnPO_4$ and $LiFePO_4$

According to the formula shown above[3]the linewidth is manly justified based on the contribution from hyperfine coupling value(A/h) and the spin lattice relaxation of the electrons(T_{1e}) [6]. However, for material studies here, the changes in the

linewidth are governed mainly by T_{1e} term. As the redox charge is raised from Fe^{2+} to Fe^{3+}, the spin number goes from S = 2 to S = 5/2) the T_{1e} decrease. And this shorter T_{1e} times of the spin density on the metal center would resulting in the observed narrower resonances. [4]

Figure 4.13 shows the comparison of ^{7}Li MAS spectrum for $LiMnPO_4$ and $LiFePO_4$ at 25kHz, we noticed that $LiMnPO_4$ has an additional unpaired electron in the t_{2g} orbital as compared to $LiFePO_4$, and it clearly shows that $LiMnPO_4$ has much higher resolution and narrow resonance. The Full-Width at Half-Maximum(FWHM) of the isotropic peak for $LiMnPO_4$ is 500Hz while for $LiFePO_4$ it is much broad at about 9000Hz. That's, once again, is due to the shorter T_{1e} times of the spin density on the metal center when compared $LiMnPO_4$ to $LiFePO_4$. As we know, Fe^{3+} has the same spin number and electron configuration with Mn^{2+} ($t_{2g}^{3}e_{g}^{2}$), which means a much narrow linewidth should be observed in^{7}Li MAS spectra for Li site close to Fe^{3+} compare to Li site close to Fe^{2+}. Therefore, we should able to identify Li signal from Fe^{3+} and Fe^{2+} easily in ^{7}Li MAS spectrum, since Li site surrounded by Fe^{3+} should have narrow linewidth, while Li site surrounded by Fe^{2+} should have very broad linewidth.

The series of MAS spectra for cycled $LixFeP_2O_7$ shows a clear trend that the signal intensities for broad resonance(arising from Li site around Fe^{2+}) will increase,

while the signal intensities for narrow resonance (arising from Li site around Fe^{3+}) will decrease, with the increase of x value(number of Li remain), and the appearance of narrow resonance are only observed for $LixFeP_2O_7$ samples with $x < 1.4$. The trend observed is the existence of both Fe^{3+} and Fe^{2+} in the electrochemical process between $LiFeP_2O_7$ and $Li_{1.4}FeP_2O_7$, and as more and more Li ion been extracted, the relative intensities between resonance arising from Fe^{3+} to Fe^{2+} keep increase.

There is no observed change to the paramagnetic shift of the cycled sample for those narrow resonance, indicating that no new Li sites near Fe^{3+} have emerged in spite of electron changes at the transition metal center. However, there is an observation of new broad resonance coming out when x = 1-1.4, which is attribute to the structure rearrangement during cycling, and these new Li site near iron in oxidation 2+ arise. This result is similar to the ex situ X-ray diffractograms study by Shimizu.et.al as they began to see new peaks around these same areas[7] .

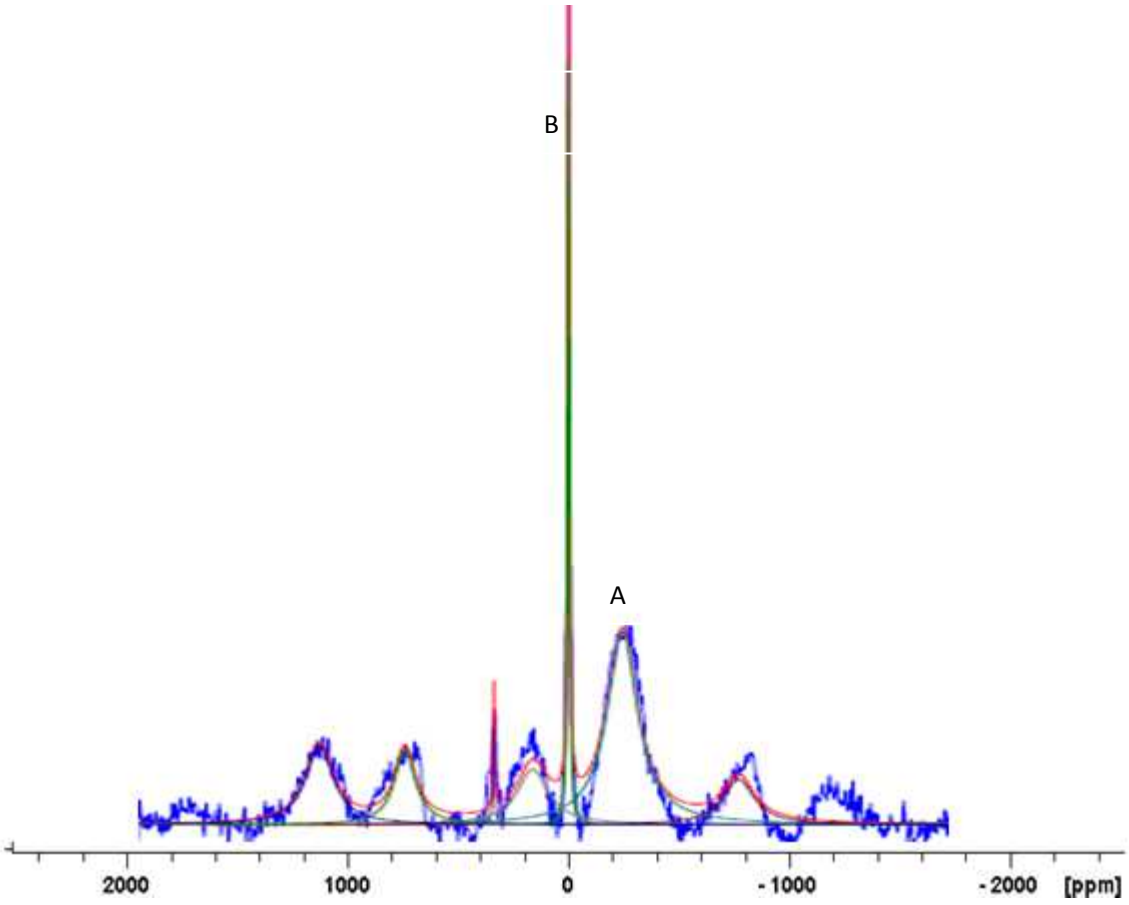

Figure 4.14-Deconvolution of ^{7}Li NMR spectrum of the $Li_{1.3}FeP_2O_7$

Here, detailed information regarding the $Li_2FeP_2O_7$ phase interface is obtained from those series of ^{7}Li MAS spectrum. The deconvolution of $Li_{1.3}FeP_2O_7$ resulting in the appearance of multiple peaks(Figure 4.14). Both “narrow” resonance arising from Li site close to Fe^{3+} and “broad” resonance arising from Li site close to Fe^{2+} are observed in this spectra. Peak A is broad with parameters similar to that of the ^{7}Li MAS NMR spectrum of pristine $Li_2FeP_2O_7$ and is thus assigned as Li sitting close to

Fe^{2+}, Peak B is very narrow and the narrowness and appearance in higher order sidebands suggests that these resonances arise due to their closeness to an Fe^{3+} environment. The integration values for both “narrow” and “broad” resonance were then obtained based on the deconvolution of the spectrum. And the totally integration result for narrow and broad resonance is shown in Figure 4.15 as well. The stopping points for the cycled cathode is shown at electrochemical curve, and the chart below indicates a clearly trend for the integration values for resonance arising from Fe^{3+} and Fe^{2+}. When the $Li_2FeP_2O_7$ cathode begin to charge from x = 2 to x = 1, before x = 1.4, only broad resonance is able to observe. When x < 1.4, with more and more Li ion being extracted, the integration values for resonance arising from Fe^{3+} keeps decreasing, while the integration values for resonance arising from Fe^{3+} keeps increasing. When the cathode begin to discharge, the opposite trend is observed and shown in the chart as well.

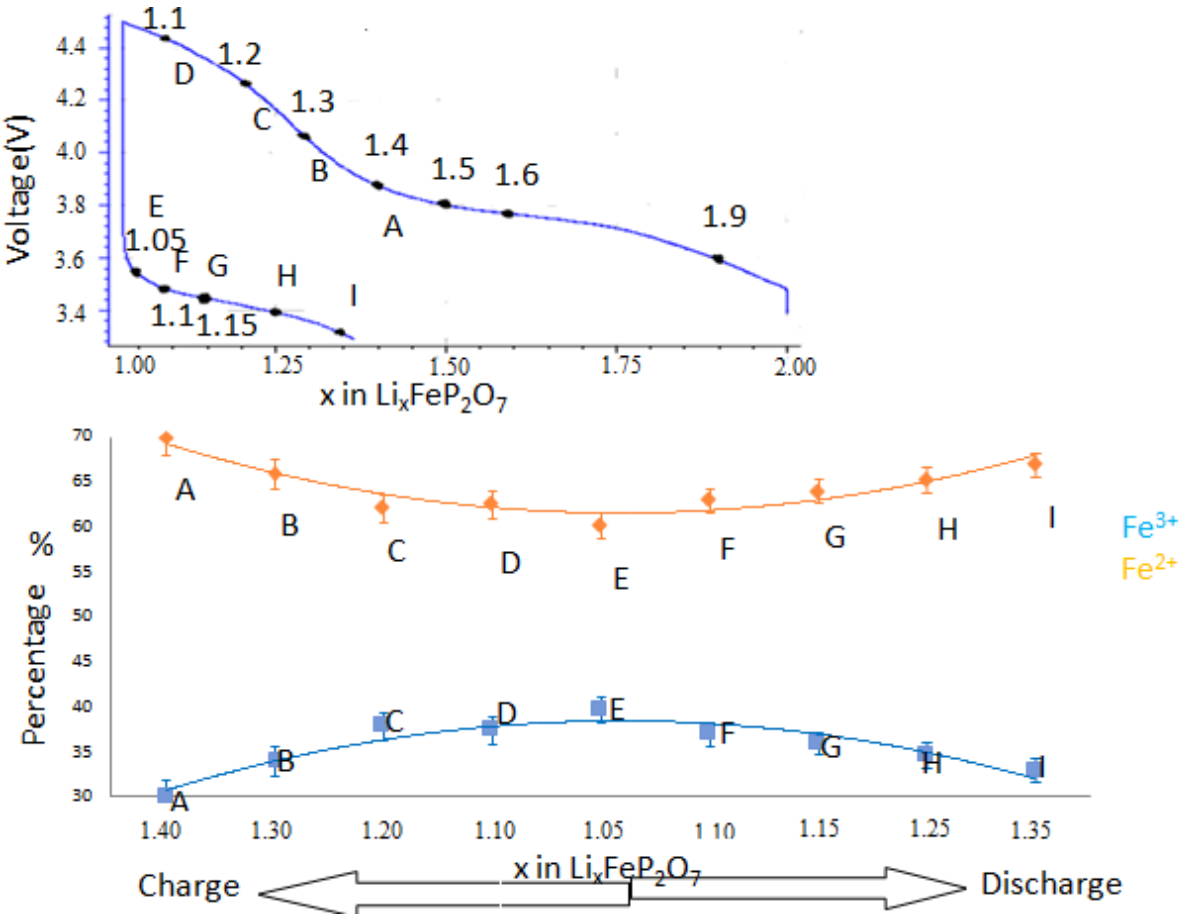

Figure 4.15- electrochemical experiments of the coin cells for $Li_2FeP_2O_7$ with the stopping shown on the figure(above), Relative Integration values for "narrow" peaks(Fe^{3+}) and "broad" peaks(Fe^{2+}) (bottom)

Figure 4.17 shows the ^7Li MAS NMR spectra of $LiFeP_2O_7$[9] , when we compared this spectra to what we observed in our series of MAS spectrum of $LixFeP_2O_7$, the linewidth and lineshape is just the same as the narrow resonance in our spectrum, which confirm that Li nuclei are sitting close to Fe^{3+} center. Since the

chemical shift of ^{7}Li isotropic peak(162ppm) they shown in the spectra of $LiFeP_2O_7$ is quite different from what we observed for the isotropic of narrow resonance, and the spectrum at one-electron fully discharge state is different from the spectra of $LiFeP_2O_7$, which means the electrochemical (de)lithiation process of $Li_2FeP_2O_7$ can't be a two-phase($LiFeP_2O_7$ and $Li_2FeP_2O_7$ phase) process, while it should be a solid-solution process.

Figure 4.17 shows the local lithium environment for those 4 Li sites in $Li_2FeP_2O_7$ where each Li ion is connected via O to Fe atoms. Oxidation of an Fe atom involved in the 90 degree orbital configuration would lead to the greatest increase in the paramagnetic shifts based on the geometry dependent delocalization of unpaired electron spin density discussed previously. Alternatively, oxidation of Fe atoms far away from 90 degree would have a less significant impact on the paramagnetic shift but through-space effects would still be observed.

Atoms	Distance(Å)
Li1-Fe1(A)	3.139
Li1-Fe1(B)	2.997

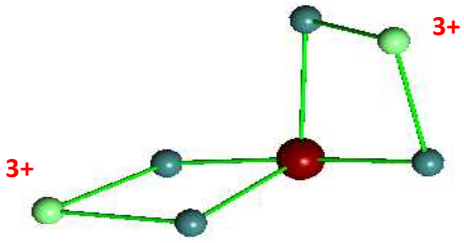

Figure 4.16-Schematic detailing the local Li environment with respect to Fe transition metal center proximity for $LiFeP_2O_7$. Left: geometry data for Li site ; Right: Local Li environments for lithium site

Atoms	Angels(˚)
Li1-O-Fe1(A)	103.33
Li1-O-Fe1(A)	97.55
Li1-O-Fe1(B)	94.67
Li1-O-Fe1(B)	97.02

Atoms	Distance(Å)
Li1-Fe1(A)	3.173
Li1-Fe1(B)	3.804
Li1-Fe2	3.448

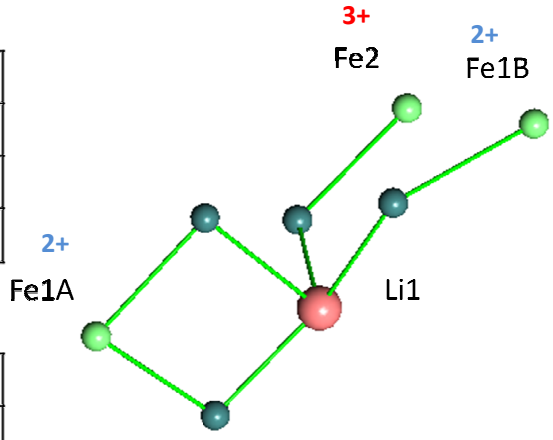

Atoms	Angel(˚)
Li1-O-Fe1(A)	90.98/108.8
Li1-O-Fe1(B)	117.43
Li1-O-Fe2	118.74

Atoms	Distance(Å)
Li2-Fe2(A)	3.196
Li2-Fe2(B)	3.976
Li2-Fe2	4.392
Li2-Fe3	3.182

Atoms	Angels(°)
Li2-O-Fe2(A)	101.21
Li2-O-Fe2(B)	113.09
Li2-O-Fe2	132.72
Li2-O-Fe3	109.32

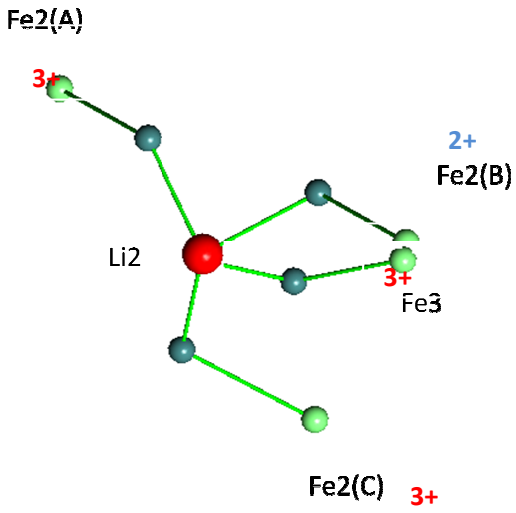

Atoms	Distance(A)
Li3-Fe1	2.942
Li3-Fe2	3.712

Atoms	Angels
Li3-O-Fe1	89.96/93.04
Li3-O-Fe2	111.59

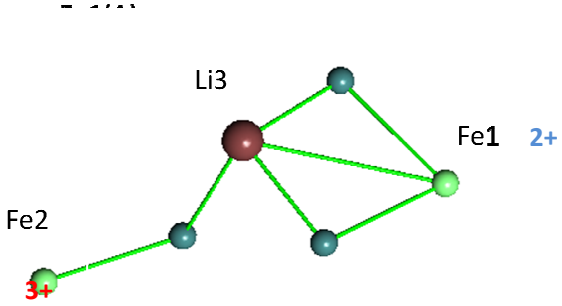

2+

Atoms	Distance(A)
Li4-Fe1	3.221
Li4-Fe2	3.266

Atoms	Angels
Li4-O-Fe1	99.71/92.54
Li4-O-Fe2	97.23/95.20

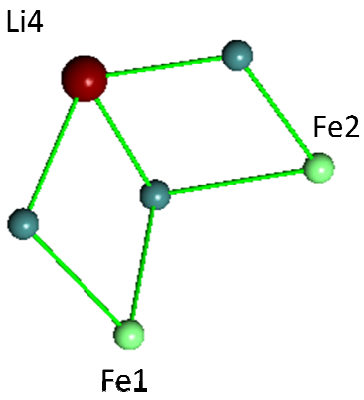

Figure 4.17-Schematic detailing the local Li environment with respect to Fe transition metal center proximity for $Li_2FeP_2O_7$. Left: geometry data for 4 Li sites ; Right: Local Li environments for each lithium site

Three unique Fe atoms are observed in the $Li_2FeP_2O_7$ structure. Those Fe atom should all in the state of Fe^{2+} in the pristine material. When the $Li_xFeP_2O_7$ cathode cycled from x = 2 to x = 1, with more and more lithium ion extracted out, the charge for some Fe atom would change from Fe^{2+} to Fe^{3+}, and we believe Fe3 and those Fe2 which is not setting close to Li4 should turn to 3+ first, and give rise to the "narrow" signal coming from both Li3 and Li2. As it shown in Figure 4.17, two of the Fe atoms turnd to Fe^{3+} , and have Li-O-Fe overlap at angles quite away from 90˚ for Li2, and one of the Fe atoms turnd to Fe^{3+} , and also, have Li-O-Fe

overlap at angles quite away from 90˚ for Li3. Since those Li-O-Fe angles are more than 100˚, those Fe^{3+} will have a very small impact on paramagnetic shift but still have similar impact on line shape and breadth of CSA, which corresponding to the narrow resonance we observed in our series of MAS spectrum near 0ppm. Since the other Fe atoms(Fe1 and some Fe2) are at the charge of Fe^{2+}, Li1, Li4 thus assigned to have environment generated where still mostly surrounded by Fe^{2+} atoms in the Li-coordination sphere, which will lead to "broad" resonance shown in the ^{7}Li spectrum. Therefore, the "narrow" signal in the series of ^{7}Li MAS spectrum should arise from Li2 and Li3, while the "broad" signal should come from Li1 and Li4. The "narrow" resonance has shown a quite similar linewidth compared to the ^{7}Li signal observed in $LiFeP_2O_7$ MAS spectra, but a different chemical shift, that's because of the poor Li-O-Fe overlap for Li2 and Li3 that lead to much less paramagnetic effect in $Li_2FeP_2O_7$ compared to $LiFeP_2O_7$. As for $LiFeP_2O_7$, if we looked at the Li local environment, three Li-O-Fe angles are closed to 90˚ with reasonable Li-Fe and Li-O nuclei distance, which will transfer positive electron spin density to the Li ion, and give rise to the chemical shift to Li site(162ppm). While for $Li_2FeP_2O_7$, poor Li-O-Fe overlap leads to almost no positive electron spin density being able to transfer to Li ions, that's why those Li sites(narrow signal) observed in (de)lithiated samples are closed to 0ppm. When

we look at the structure of delithiated cathode, as it shown in figure 4.18, it's obviously that we are observing Fe^{2+} and Fe^{3+} mixing throughout the structure instead of separate domains of Fe^{2+} and Fe^{3+} , which confirmes a solid-solution process during electrochemical cycling.

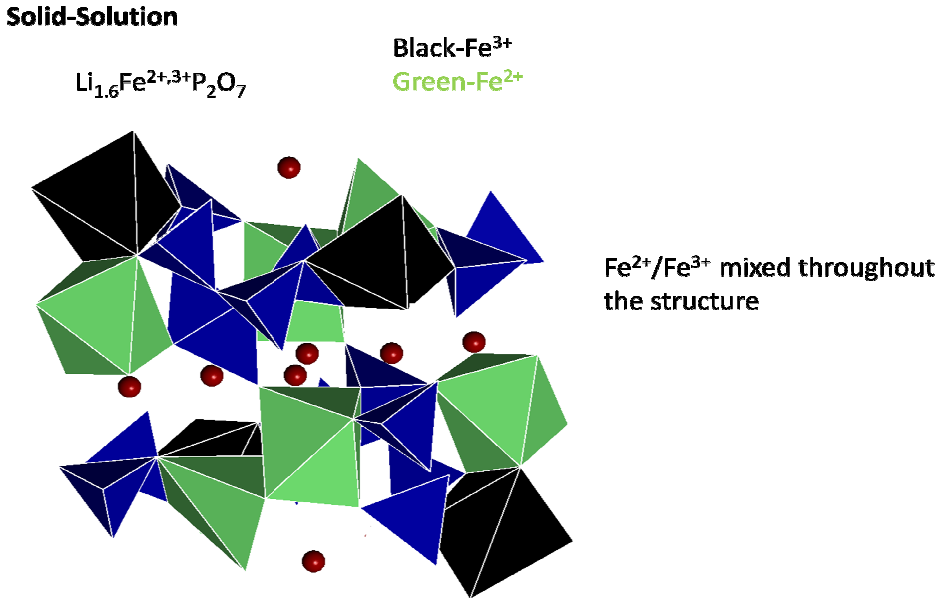

Figure 4.18-Structure of $Li_{1.6}FeP_2O_7$, one unit cell

4.4 Summary

$Li_2FeP_2O_7$ pyrophosphate is the latest phosphate-based polyanionic cathode material with a high redox potential at 3.5 V. This chapter presents the first NMR study of $Li_2FeP_2O_7$. What also present here is the MAS NMR study for (de)lithiated $Li_xFeP_2O_7$ sample during electrochemical cycling. The ex-situ NMR study indicates that the electrochemical redox mechanism of $Li_2FeP_2O_7$ involves a single-phase, solid-solution mechanism. The electrochemical (de)lithiation of $Li_xFeP_2O_7$ probably involves structural rearrangement as new resonance was observed in the spectrum.

Future studies could not only increase the number of cycled cathode used for NMR study, but also utilize 1D variable temperature experiment as well as 1D selective inversion methods for determining ion hopping rates. Details of the selective inversion experiments and how they can be applied to paramagnetic systems are outlined in chapter 2 and 3.

4.5 References

(1) Zhou, H., et al., Chemistry of Materials, 2010. 23(2): p. 293-300.

(2) Nishimaru, S. et a., Chemistry of Materials, 2010. 132: p.13596-13597

(3) Andersson, A.S.; Kalska, B; Solid State Ionics. 2000, 173, 21

(4)Kim, H, Chemistry of Materials, 2011, 23, 3930

(5)Padhi, A.K.; J.Electrochem. Soc. 1997, 144, 1188

(6)Andersson, A.S.; Kalska, B; Solid State Ionics. 2000, 130, 41

(7)Takahashi, T. K. Solid State Nuclear Magnetic Resonance. 1999, 15, 119

(8)Shimizu, D. et al., Chemistry of Materials, 2012. 24: p.2598-2603

(9)Andersson, A. S.; Kalska, B; Chemistry of Materials, 2000, 10, 1542

Chapter 5: Summary and Future direction

Since the commercialization of lithium-ion batteries in the 1990s, they have undergone intensive scientific research and successful applications in a variety of portable electronic devices. However, to apply current lithium ion battery systems towards larger scale application, such as EVs, many of the cost and safety issues of the current systems still need to be addressed, and most important, ideal cathode material with high energy density, low cost, fast cycling rate is needed. In order to better understand the mechanisms of these new cathode materials for lithium ion batteries, not only the local lithium structural information, but also the lithium ion pathway as well as the ion mobility are needed to be clearly understood. Current widely used XRD technique is definitely a powerful tool for understanding these structures, however its low sensitivity to small atoms such as Li do limit its accuracy. Multinuclear solid-state NMR is a tool that is sensitive to local environments of mobile ion, and it can give us information regarding ion dynamics, which can then be used to determine the timescales and energy barriers of ion mobility in the multi-Li site materials.

This thesis presented ^{6,7}Li solid-state NMR results that elucidated the structural and Li ion mobility properties in a series of lithium pyrophosphate compounds used as

cathode materials for Li ion batteries. NMR of these materials is made non-trivial by the strong through-bond and through-space coupling between the nuclei being measured and the unpaired electron spin density sitting on the transition metal center. This thesis also managed to expand the number of NMR tools available to study ion dynamics in cathode materials. Previous studies of Li ion mobility have used ^{6,7}Li 2D EXSY measurements over a variable temperature range to quantify ion hopping rates and energy barriers in paramagnetic Li counpounds[1][2]. Analysis of this data is most accurate when the longest mixing time extends well beyond the correlation time of the exchange process. However, in strongly paramagnetic systems such as those studied here, short spin-lattice relaxation of the Li nuclei limits the range of mixing times available leading to a more complicated data analysis. This thesis showed that ^{6}Li Selective Inversion experiments are an excellent alternative means to measure ion dynamics in solid-state paramagnetic materials, especially in systems where the ion hopping rates are slow relative to the spin-lattice time of the Li nuclei. Here, a chapter-by-chapter breakdown of the key results from each section is given with suggestion for future work included.

Chapter 3 detailed the characterization of the structure and ion mobility properties of the $Li_2MnP_2O_7$ using ^{7}Li MAS NMR measurements. Those $Li_2MnP_2O_7$ samples were synthesized in our group using a convenient solid-state reaction,

allowing for ^{6,7}Li MAS NMR measurements of this material. The lithium environments in $Li_2MnP_2O_7$ are studied and Li resonances are assigned initially based on the Fermi-contact interaction with the paramagnetic Mn center, which has been further confirmed by the dynamic studies. ^{6}Li 1D shaped pulsed selective inversion measurements were applied to $Li_2MnP_2O_7$ in order to determine the ion hopping rates over a variable temperature range. It has subsequently expanded the NMR tools available to study ion mobility timescales in this class of materials. In the four-site material, $Li_2MnP_2O_7$, only exchange pairs AB and CD are identified to be possible through crystal structure analysis of $Li_2MnP_2O_7$. ^{6}Li selective inversion measurements using shaped pulses are used to quantify the hopping rates through a series of experiments over a variable temperature range for exchange pair CD. The CIFIT rate matrix used to fit the experimental data included variables for exchange processes. Because of the small chemical shifts separation in $Li_2MnP_2O_7$, it gives a great challenge to optimize the selective inversion pulse to reach a inversion that has an smallest effect on non-inverted sites. A series of different initial conditions for selective inversion pulses have been applied, and the rates of the exchange pairs determined. It is shown that the ion hopping rates are not altered outside the errors bounds given when changing the initial conditions for selective inversion pulses. It was concluded that selective inversion measurements using shaped pulses is an

accurate method for determining ion exchange rates in solid-state paramagnetic materials. The ion hopping rates for CD exchange pair in $Li_2MnP_2O_7$ is found to be on a similar timescale to those determined previously for Li_2VPO_4F, and shows a slower timescales of ion mobility than the phosphates $LiFePO_4$, $Li_3Fe_2(PO_4)_3$.

Dynamic studies on $Li_2MnP_2O_7$ may be extended to other lithium pyrophosphate materials such as $Li_2FeP_2O_7$, $Li_2VP_2O_7$ and $Li_2(Fe_{1-y}Mn_y)P_2O_7$, as these materials all have quite similar crystal structure. Even though at this moment, the electrochemical performance of $Li_2MnP_2O_7$ is not satisfactory, the cyclic voltammetry studies for $Li_2MnP_2O_7$ have shown two oxidation peaks at 4.5V and 5.3V, which is extremely high and should corresponding to Mn^{2+}/Mn^{3+} and Mn^{3+}/Mn^{4+} redox couples. And recent studies on $Li_{2-x}(Fe_{1-y}Mn_y)P_2O_7$ mixed- metal pyrophosphate materials have shown that the inclusion of Mn is able to push the Fe^{3+}/Fe^{2+} redox potential close to 4 V. The $Li_2MnP_2O_7$ behaves quite similar to the olivine structure $LiMnPO_4$, which also has high redox potential (4.1V) and poor electrochemical performance when first discovered. However, after plenty of attempts by different groups trying to improve its electrochemical cyclability using a series of techniques like carbon coating and nanosizing, it is finally able to push the specific capacity to almost 150mAh/g (Theoretical capacity 171mAh/g), and make it a promising candidate as cathode material for lithium ion batteries.

The future work on $Li_2MnP_2O_7$ should include low-temperature dynamic studies using experiments like selective inversion or 2D-EXSY. As it shown in the variable temperature studies, cooling the sample to a very low temperature do increase the resolution and gives a larger peak separation in the spectrum, which would make it easier for dynamic studies using currently methods and achieve more accurate ion hopping rates.

In Chapter 4, $Li_2FeP_2O_7$ has been choose as targeted material and been studied using ^{7}Li MAS NMR. This chapter presents the first NMR spectrum of $Li_2FeP_2O_7$, a preliminary deconvolution has been made trying to understand the local lithium environments in $Li_2FeP_2O_7$. Chapter 4 also presents the MAS NMR study for (de)lithiated $Li_xFeP_2O_7$(x from 1 – 2) sample during electrochemical cycling. The NMR spectra for $LiFeP_2O_7$ was already obtained by other groups[3] and the isotropic peaks arising from Fe^{3+} are narrow. While in the NMR spectrum of (de)lithiated $Li_xFeP_2O_7$ sample, both narrow and broad resonance are observed. It is possible that this broadening is due to the change in T_{1e} at the paramagnetic center brought on by the change in Fe oxidation state. A lengthened T_{1e} could greatly increase the full-width half-max(FWHM) of the isotropic Li lineshapes. Li near a Fe^{3+} site should corresponding to a narrow resonance, while Li near a Fe^{2+} site should corresponding to a broad resonance. Since the isotropic chemical shift for the Li sites arising from

Fe^{3+} in $Li_xFeP_2O_7$ (0ppm) is quite different from the isotropic chemical shift in $LiFeP_2O_7$(162ppm), the electrochemical redox mechanism of $Li_2FeP_2O_7$ can't be a distinguish two-phase reaction between $LiFeP_2O_7$ and $Li_2FeP_2O_7$ phases as reported by Kim.et.al[4], on the contrary, the ex-situ NMR study indicates that the electrochemical redox mechanism of $Li_2FeP_2O_7$ involves a single-phase, solid-solution mechanism as reported by Shimizu et,al[5].

The focus of ongoing work is using ^6Li enriched $Li_2FeP_2O_7$ sample for NMR studies. ^6Li has a smaller gyromagnetic ratio compared to ^7Li, which means smaller dipolar interaction and will lead to a higher resolution in Li MAS NMR spectrum. With higher resolution, we may be able to quantify the Li ion mobility timescales in the $Li_2FeP_2O_7$ phase, and it may also be interesting to know how the ion dynamics are changed in (de)lithiated sample $Li_xFeP_2O_7$ (x = 1 – 2). Quantification of the timescales ^6Li Selective Inversion measurements and 2D-EXSY are proposed as a continuation of this project.

Recently, Furuta.et.al has reported the synthesis and electrochemical properties of mixed-metal pyrophosphates, $Li_2(Fe_{1-y}Mn_y)P_2O_7$[6]. The samples were synthesized by an optimized solid-state route. They form a complete solid solution assuming a monoclinic framework with space group $P2_1/c$. The electrochemical analysis show that when gradual substitution of Mn into parent $Li_2FeP_2O_7$ phase triggered a splitting

of Fe^{3+}/Fe^{2+} redox peak and partial upshifting in Fe^{3+}/Fe^{2+} redox potentials nearing 4.0 V, which is very promising. So another future works of this project should be using ^{6,7}Li solid-state NMR to study this mixed-metal pyrophosphates, as we already known from our work in this thesis that the $Li_2MnP_2O_7$ phase has higher resolution in NMR spectrum, and $Li_2FeP_2O_7$ phase has better electrochemical performance. And it may be quite interesting to see what information can SSNMR get from these mixed-metal pyrophosphates, $Li_2(Fe_{1-y}Mn_y)P_2O_7$.

Solid-state NMR methods are effective tools for characterizing both the structural and ion mobility properties of cathode materials for Li ion batteries. This thesis focused on Li ion cathode materials with pyrophosphate anion compositions. By measuring the ion mobility timescales and studying electrochemical cycled samples using solid-state NMR methods, it will help us develop cathode materials with lower cost and better performance.

5.2 References

(1) Cahill, L.S., Chapman, R. P., Britten, J. F., Goward, G. R., Journal of Physical Chemistry B, 2 006. 110: p. 7171-7177.

(2) Davis, L.J.M., I. Heinmaa, and G.R. Goward, Chemistry of Materials, 2010. 22(3): p.769-775.

(3) Andersson, A. S.; Kalska, B; Chemistry of Materials, 2000, 10, 1542

(4) Kim, H, Chemistry of Materials, 2011, 23: p.3930-3932

(5) Shimizu, D. et al., Chemistry of Materials, 2012. 24: p.2598-2603

(6) Naoya Furuta. et al., Chemistry of Materials, 2012. 24:p.1055-1061